Global environmental constraints on magnetic reconnection at the magnetopause from in-situ measurements

B. Michotte de Welle[1], N. Aunai[1], B. Lavraud[2], V. Génot[3], G. Nguyen[4], A. Ghisalberti[1], A. Jeandet[1], Roch Smets[1]

[1]CNRS, Ecole polytechnique, Sorbonne Université, Université Paris Sud, Observatoire de Paris, Institut Polytechnique de Paris, Université Paris-Saclay, PSL Research Univsersity, Laboratoire de Physique des Plasmas, Palaiseau, France
[2]Laboratoire d'Astrophysique de Bordeaux, Université Bordeaux, CNRS, Pessac, France
[3]Institut de Recherche en Astrophysique et Planétologie, CNRS, Université de Toulouse, CNES, Toulouse, France
[4]ONERA, France

Key Points:

- Reconstruction of the magnetic shear, current density, and asymmetric reconnection rate at the magnetopause using in-situ measurements.
- Parametric study of spatial distributions as a function of interplanetary magnetic field and dipole tilt orientations.
- Comparison of the local orientation of magnetic reconnection predicted by global constraints to that suggested by local simulation studies.

Corresponding author: B. Michotte de Welle, bayane.michotte-de-welle@lpp.ploytechnique.fr

Abstract

Magnetic reconnection is the main driver of the magnetospheric activity. When it occurs at the magnetopause, it couples the magnetosphere with the interplanetary medium, enabling transport from the solar wind into the otherwise confined cavity. The efficiency of this coupling critically depends on the location on the magnetopause where reconnection takes places. Several models have been proposed regarding where the reconnection could locate but on the one hand, none is always supported by global simulations, an on the other hand, observations from in-situ measurements have remained too scarce to approach the problem in detail from a global and parametric standpoint. In this work, we investigate how the spatial distributions of physical quantities known to be important in the magnetic process might constrain the location of global X-lines at the magnetopause. We use in-situ measurements from four missions (Cluster, Doublestar, THEMIS, MMS), automatically selected using statistical learning, to reconstruct the global distribution of the magnetic shear angle, current density, and asymmetric reconnection rate at the dayside magnetopause. The comparison of the magnetic shear maps from in-situ measurements with those obtained with magnetic field models reveals important spatial discrepancies for a certain range of IMF cone angles ($12.5^\circ \pm 2.5^\circ \leq |\theta_{co}| \leq 45^\circ \pm 5^\circ$), but also a difference in the behavior of the lines maximizing this quantity with respect to the IMF clock angle. The parametric study of the effect of the IMF orientation and the dipole tilt angle shows that the IMF cone angle creates strong asymmetries in the distribution of the above-mentioned quantities and changes their dependence on the IMF clock and the dipole tilt angles. Finally, we show that the X-line constructed by maximizing a given quantity gives local orientations of magnetic reconnection that are inconsistent with the predictions suggested by local simulation studies.

1 Introduction

Magnetic reconnection is the primary driver of the magnetospheric activity (Baumjohann & et al., 2012; Cassak & Fuselier, 2016). On the magnetopause, observational evidences indicate it could occur along an extended line (Phan et al., 2000, 2001, 2006; Dunlop et al., 2011; Zhou et al., 2017; Walsh et al., 2017). Such a long X-line has also been seen in global magnetohydrodynamic (MHD) simulations (Komar et al., 2015; Glocer et al., 2016; Souza et al., 2017; Eggington et al., 2020). However, its precise location on the magnetopause, as a function of solar wind and interplanetary magnetic field (IMF) conditions remains a challenging open question. Determining that location is crucial, as the efficiency of reconnection strongly depends on the local properties of the plasma and the magnetic field (Axford, 1969; Vasyliunas, 1975; Cassak & Shay, 2007; Borovsky et al., 2008; Borovsky & Birn, 2014), which significantly vary along the magnetopause surface (Dimmock & Nykyri, 2013; Dimmock et al., 2014, 2016; Zhang et al., 2019). Historically, the X-line was considered to locate only in regions separating anti-parallel magnetic fields (Dungey, 1961; Crooker, 1979; Luhmann et al., 1984). Numerous observations (e.g. (Daly et al., 1984; Scurry et al., 1994; Pu et al., 2005)) of reconnection signatures consistent with the merging of only components of the field, however, later favored the alternative idea of possible non-coplanar merging (Sonnerup, 1974; Gonzalez & Mozer, 1974; Hill, 1975; Cowley & Owen, 1989; Cooling et al., 2001; Moore et al., 2002). The reconnection of non-coplanar magnetic fields, however, vastly complicates the problem of locating the X-line, enabling it to explore much wider range of conditions and locations on the magnetopause surface. Several studies have then be dedicated to finding physical effects and observational evidences that would help narrowing down the possible regions where X-lines could be found on the magnetopause.

Observations and analysis of low-speed cutoff in cusp ion distributions (Onsager et al., 1991), and later of ion flow reversals (Trattner et al., 2017, 2021), were found to correlate well with regions on the magnetopause were analytical models predict a large magnetic shear. This led to the empirical proposition that, given a global map of the mag-

netic shear for some IMF orientation and dipole tilt angle, the X-line is a global line traversing regions maximizing the shear angle. More specifically, the so-called *Maximum Magnetic Shear model*, predicts that, for strongly southward IMF ($155^\circ < \theta_{cl} \equiv \tan^{-1}(B_y/B_z) < 205^\circ$ with $\theta_{cl} \in [0, 2\pi]$) or for a dominant B_x component ($B_x/\|\mathbf{B}\| > 0.7$), the X-line would be localized in anti-parallel regions. For other conditions, the X-line would mostly traverse the dayside magnetopause where the shear is maximum to join anti-parallel regions in the flanks (Trattner et al., 2016, 2021).

The maximum shear model has difficulties explaining reconnection signatures observed at times where the IMF shows a dominant B_x component (typically when the IMF cone angle $\theta_{co} = \tan^{-1}\left(\sqrt{B_y^2 + B_z^2}/B_x\right)$ is less than 45°) (Trattner et al., 2021). A possible explanation for these difficulties stands in the inacurate draping predicted by the Kobel & Fluckiger current-free magnetostatic model (Kobel & Fluckiger, 1994), hereafter noted as KF94, at the root of the shear maps used to compute the X-line location (Trattner et al., 2012a, 2021). Recent work by Michotte de Welle et al. 2022 (Michotte de Welle et al., 2022) revealed that the 3D magnetic draping reconstructed from in-situ measurements indeed significantly differs from the magnetostatic predictions for conditions where the IMF cone angle $|\theta_{co}|$ is comprised between $12.5^\circ \pm 2.5^\circ$ and $45.0^\circ \pm 5^\circ$, owing to the important role of the plasma flow in the magnetosheath.

Besides observational evidences at the root of the model, maximizing the magnetic shear also makes sense from a theoretical perspective if considering reconnection lies in regions that are the most favorable for either its onset or fast reconnection rates, and if maximum magnetic shear regions are seen as a good proxy of these locations. However, both the onset via the tearing instability (Drake & Lee, 1977; Daughton & Karimabadi, 2005), and fast reconnection rates in the nonlinear regime, more fundamentally depend on other quantities such as the current (Alexeev et al., 1998) and plasma densities and the magnetic field amplitude jump across the magnetopause (*Reconnection of Magnetic Fields: Magnetohydrodynamics and Collisionless Theory and Observations*, 2007). These parameters, despite their obvious correlation with the magnetic shear, have, a priori, no reason to be distributed along the magnetopause surface exactly the same way. In other words, regions maximizing the magnetic shear may not be those where the current density or the reconnection rate are the most favorable for either the onset or a fast reconnection rate. Realistic spatial distributions of these more fundamental quantities are, however, more difficult to obtain than that of the magnetic shear. Today, such global distributions are obtained from global MHD simulations. A study based on global MHD simulations (Komar et al., 2015) have shown that the self consistent topological separator along which reconnection occurs often correlates well with the maximization of the current density, the magnetic shear or reconnection rate (Borovsky, 2013) and outflow speed scaling laws (Swisdak & Drake, 2007). However, the IMF and dipole configurations that were used did not result in significant differences among the various theoretical predictions. Results also showed cases, such as for northward IMF with an important dipole tilt angle, where none of the lines maximizing the above quantities were consistent with the topological separator obtained in the simulation. Finding conditions where the maximization of the above quantities leads to well-differentiated predictions will require computationally heavy parametric studies, with a deeper exploration of the role of the IMF cone angle and the tilt of the geomagnetic dipole, which are still poorly understood despite their likely importance.

It is important to note that above ideas, consisting in the construction of an X-line on the magnetopause surface from the maximization of a specific quantity, given its spatial distribution on the magnetopause, *de facto* also imposes the local orientation of that X-line with respect to the magnetic field on each side of the boundary at that location. In this paradigm, that we shall identify as the *global approach* to the localization problem, the local orientation of an X-line, can thus only be determined with the knowledge of the global state of the magnetopause. Interestingly, however, simulations of isolated

asymmetric current sheets separating magnetic field sheared by some arbitrary but uniform angle (Swisdak et al., 2003; Hesse et al., 2013; Y.-H. Liu et al., 2015; Aunai et al., 2016; Y.-H. Liu et al., 2018), still end up with an X-line aligned with a specific orientation, which, in this case, can only result from local physics, which is, moreover, often neglected in global MHD models. The mechanisms imagined to constrain the local orientation of an X-line in this approach incidentally also follow the idea consisting in maximizing the efficiency of the process. Several effects have been considered, which are not mutually exclusive, such as the diamagnetic drift of the X-line (Swisdak et al., 2003), the importance of the "magnetic energy" available in the reconnecting components (Hesse et al., 2013), the preferred orientation of tearing modes (Y.-H. Liu et al., 2015, 2018), or maximizing the outflow velocity (Swisdak & Drake, 2007). These studies can be gathered into what we shall call the *local approach* to the localization problem, for which a global line would result from following local orientations determined by such local effects. This local approach has already been considered in a previous work (Moore et al., 2002) where a global line results from following the local bisector of analytical models of the magnetic field in the magnetosheath and magnetosphere. Interestingly, the orientation of the bisection, followed somewhat arbitrarily in the aforementioned study, has later been found in several self consistent 2D and 3D full and hybrid PIC simulations as the one favoring the fastest rate of all orientations (Hesse et al., 2013; Y.-H. Liu et al., 2015; Aunai et al., 2016; Y.-H. Liu et al., 2018).

Whether it concerns the local or the global approach, the spatial distribution of key quantities on the magnetopause usually emanates from analytical or numerical models and remains largely unknown from an observational standpoint. The recent reconstruction of the magnetic field draping throughout the global magnetosheath (Michotte de Welle et al., 2022), and in particular adjacent to the magnetopause, from large statistical analysis of multi-mission data, has opened up an opportunity for investigating the detailed spatial distributions of these quantities and their dependence on the IMF orientation and dipole tilt angle. This study therefore aims to revisit the problem of localizing the reconnection X-line on the magnetopause, this time from in-situ measurements only, following this large-scale, multi-mission statistical analysis methodology.

The second section of this paper presents the data that has been used and explains the different steps in the statistical processing of the data. We then start by investigating to what extent magnetic shear maps obtained from magnetic field models, often used today to predict the location of X-lines, resemble those reconstructed from in-situ measurements. Section 3 establishes this comparison, for typical large, intermediate and low IMF cone angle conditions. To go beyond the sole usage of the magnetic shear, section 4 presents magnetopause maps of the current density and of what we call the *potential reconnection rate*, i.e. the rate at which reconnection would locally proceed if it was occurring there, based on the evaluation of an MHD scaling law (Cassak & Shay, 2007). These quantities are chosen for their very basic and general role in magnetic reconnection, and because they have been among the most discussed so far in the aforementioned literature. Other quantities, such as the density of cold and heavy ions populations(Toledo-Redondo et al., 2021), the plasma beta (Swisdak et al., 2003; Phan et al., 2013), the solar wind Mach number, etc. are also known to impact dayside reconnection. Taking them into account, however, shall come in a more refined version of this work at later times not to complicate the already many outcomes of this study. A possible way to include these effects while keeping the same driving idea, would be to include their impact in the reconnection rate estimate. These global maps are then analyzed for various IMF orientations and dipole tilt angles. In each of these configurations, we compute and show the X-line that maximizes the distribution of the magnetic shear, the current density and potential reconnection rate, following the global approach. We discuss how the produced X-lines vary across the various quantities, and also how they evolve with the changing of the IMF orientation and dipole tilt. Lastly, section 5 examines to what extent follow-

ing the local approach results in different X-lines than the global approach. The results are then summarized and discussed in section 6.

2 Method

This study is based on the reconstruction of the spatial distribution of the magnetic shear, the current density and potential reconnection rate on the magnetopause surface from in-situ spacecraft measurements, as a function of the IMF orientation and dipole tilt angle, from which candidate X-lines are computed following the aforementioned global and local approaches. Spacecraft measurements take the form of multivariate time series of physical quantities measured at the position of the spacecraft along their orbit. These time series can be seen as one-dimensional cuts within a three-dimensional inhomogeneous and unsteady system, thereby mixing temporal and spatial variations. The global spatial distribution of any quantity on the magnetopause is thus not readily accessible from such measurements. Our strategy, to reconstruct a global spatial distribution from these data follows the ergodic principle as previously done in Michotte de Welle et al. 2022 (Michotte de Welle et al., 2022). Namely, the sampling of a system at random positions and times, in a given configuration, can be seen as an average global representation of the system in that configuration. In our case, we assume that the numerous crossings of the magnetopause and its adjacent regions, by various spacecraft over time, and at multiple locations, within a certain proximity of a given IMF orientation and dipole tilt angle, can be used together to reconstruct the global state of the magnetopause for this IMF and dipole conditions. This is made possible by using as much data as possible and some data processing which this section aims at explaining.

2.1 Data usage

The ergodic strategy we follow requires as much data as possible measured on both sides of the magnetopause and for each of the IMF and dipole tilt angle conditions we aim at building a map for. We choose to work with the data from four missions, namely Cluster, Double Star, THEMIS and Magnetospheric MultiScale (MMS). These missions have been delivering data consistently for a large time period, on both equatorial and polar orbits, with relatively few caveats thus enabling their automatic handling. Data is used from the earliest available measurements of each mission up to 2021, time at which this work begins. For this study, we need magnetic field measurements and the ion particle density, to compute the magnetic shear angle, current density and reconnection rate scaling law. These data are basic data products available on all missions. The magnetic field is obtained from flux gate magnetometers on each spacecraft (Balogh et al., 2001; Carr et al., 2005; Auster et al., 2008; Russell et al., 2016). Particle density from Cluster 1 and 3 and Double Star is taken from Hot Ion Analyzer (HIA) when in magnetosheath or magnetospheric modes exclusively. On THEMIS, the ion particle density is taken from the Electrostatic Analyzer (ESA) (McFadden et al., 2008) in reduced fast survey mode, with on board moments (MOM) used to fill in missing ESA data. On MMS, the ion particle density is obtained from Fast Plasma Investigation (FPI) instrument (Pollock et al., 2016) in fast survey mode from the MMS 1 probe only. Particle densities and magnetic field measurements from all missions are resampled at 5 seconds resolutions on the same timestamps. We also use OMNI (King & Papitashvili, 2005) data, namely the magnetic field, plasma bulk velocity, ion particle density, ion temperature, dynamic pressure, plasma beta, Mach number, and the position of the bow shock subsolar point at 1 minute resolution from 2000 to 2021 and resample them at the same cadence as previous data. Table 1 summarizes the missions and data usage.

Mission	Probe	Period	Instruments
Cluster	C1	2001-2019	Cluster Ion Spectrometry (CIS) (Rème et al., 2001)
	C3	2001-2009	Fluxgate Magnetometer (FGM) (Balogh et al., 2001)
DoubleStar	TC1	2004-2007	Hot Ion Analyzer (HIA) (Rème et al., 2005) Fluxgate Magnetometer (FGM) (Carr et al., 2005)
Themis	A, D, E	2007-2021	Electrostatic Analyzers (ESA) (McFadden et al., 2008)
	B, C	2007-2009	Fluxgate Magnetometer (FGM) (Auster et al., 2008)
Magnetospheric Multiscale	MMS1	2015-2021	Plasma Investigation (FPI) (Pollock et al., 2016) Fluxgate Magnetometer (FGM) (Russell et al., 2016)
OMNI	N/A	2001-2021	

Table 1. Source of the in-situ data.

2.2 Extraction of the magnetosheath and magnetosphere measurements

The first step of this study consists in automatically selecting, per spacecraft, time intervals during which measurements were made in the dayside magnetosheath, or in the dayside magnetosphere, in two distinct subsets. From the equator to higher latitudes, and from the quasi-parallel to the quasi-perpendicular regions, the magnetosheath is spatially quite inhomogeneous. Moreoever, its states strongly depends on solar wind and IMF conditions (Dimmock et al., 2020). Using a set of empirically fixed thresholds on specific quantities to extract data measured in the magnetosheath is thus not optimal. Such classification task is, however, routinely and well performed by machine learning algorithms, which can easily draw complex boundaries in high dimensional parameter spaces. Recent works have, incidentally, shown that machine learning classification methods (Breuillard et al., 2020; Olshevsky et al., 2021; Nguyen et al., 2022a) can achieve excellent performance at discriminating spacecraft data based on the region they were measured in. Here, we use a gradient boosting classifier originally trained and used in Nguyen et al. 2022 (Nguyen et al., 2022a) and more recently in Michotte de Welle et al. 2022 (Michotte de Welle et al., 2022) to extract and discriminate data measured in the dayside magnetosheath and dayside magnetosphere. This algorithm has been trained to perform a point-wise classification of the data (ion density and bulk velocity, and magnetic field components) measured in the near-Earth environment according to whether they were measured in the magnetosphere, solar wind, or (if none of the above) in the magnetosheath. Using this method, we obtain about 50 and 84 millions 5-second resolution timestamps associated with data measured in the magnetosheath and magnetosphere, respectively, across all considered spacecraft. Figure 1 represents the distribution of the selected measurements for the magnetosheath and magnetosphere subsets in various cuts.

2.3 Pairing measurements with upstream solar wind properties

As previously mentioned, the state of the magnetosheath strongly depends on upstream solar wind and IMF conditions. At various steps of our data processing, and above all, in order to make a map for a specific IMF orientation, it is important to pair each measurement in the magnetosheath, to solar wind and IMF properties (magnetic field, density, temperature, velocity, dynamic pressure, Mach number, plasma beta) from the OMNI dataset (King & Papitashvili, 2005) measured at a previous time.

Solar wind properties are selected at a time shifted from the measurement time to account for the propagation up to the spacecraft. The time shift is estimated by using

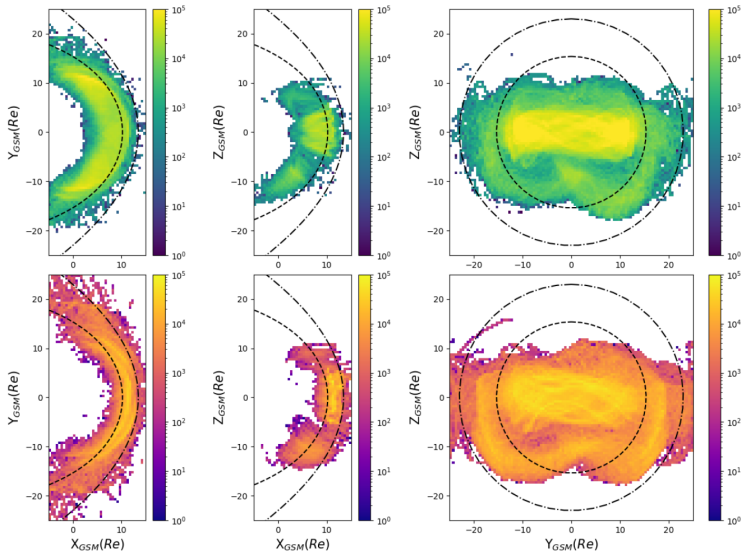

Figure 1. Distributions of selected measurements in the magnetosphere (upper panels) and the magnetosheath (lower panels) are presented with color-coding indicating the number of points per bin. The left panel displays the (X_{GSM}-Y_{GSM}) plane with data points located within $|Z_{GSM}| \leq 1R_e$. The middle panel shows the (X_{GSM}-Z_{GSM}) plane with data points located within $|Z_{GSM}| \leq 1R_e$. The right panel shows all data points in the (Y_{GSM}-Z_{GSM}) plane. The magnetopause and bow shock are represented by dashed and dash-dotted black lines, respectively.

a propagation method adapted from Safrankova et al. 2002 (Safránková et al., 2002). We first estimate the distance, along the Earth-Sun line, between the nose of the bow shock (at which OMNI data is defined) and the spacecraft position. The propagation time between these positions is then estimated based on an average solar wind speed. The solar wind velocity is taken from OMNI data as the average over a 5 minutes window centered around the measurement time to which is substracted the computed time shift. A new time shift is then estimated based on that new solar wind speed, and then used, as previously, to obtain final values of solar wind and IMF parameters. Further iterations could be made but represent a significant overhead in the execution of the overall pipeline, since this procedure is required for each of the 50 millions magnetosheath data points. The consistency of the results we obtain justify, *a posteriori*, this is enough, but other applications may require a more detailed selection. Measurements for which no OMNI data exist are discarded from the dataset and we obtain after the pairing process, a total of 46 and 75 million points of magnetosheath and magnetosphere measurements, respectively.

2.4 Repositioning of measurements relative to the magnetopause and bow shock

In order to reconstruct magnetopause maps, we need to use only those measurements that were made close-by the magnetopause. This is not trivial, for two main reasons. First, due to the rapid motion of the magnetopause, two measurements made at the same time interval from their closest magnetopause crossing have not necessarily been made at the same distance from it. Then, two points in the dataset with the same absolute position, may very well be at vastly different distances from the magnetopause owing to the possibly very different solar wind and IMF conditions at the time they were measured. Keeping measurements where they are, as they appear on Fig. 1, would blur

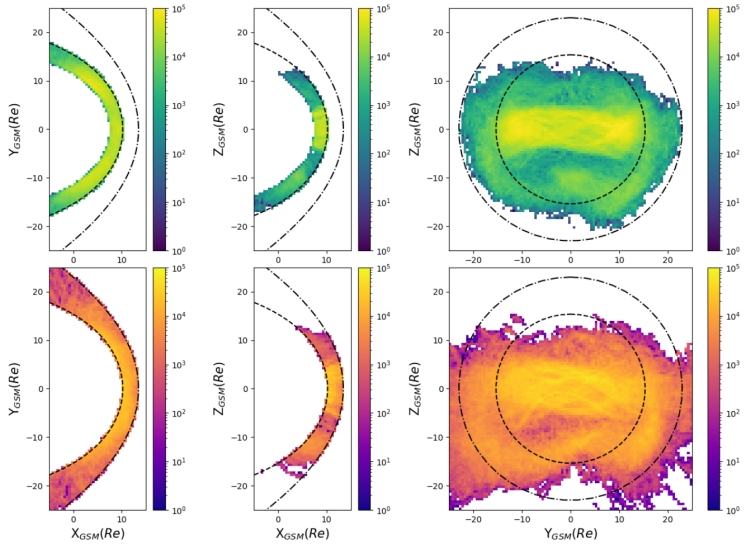

Figure 2. Distributions of magnetosphere (upper panels) and magnetosheath (lower panels) data point positions after re-normalization, presented through color-coded bins indicating the number of points per bin. Format is the same as Fig. 1.

the spatial variations by mixing, locally, values that should rather be located at different positions. Measurements thus need to be re-positioned at their "true" location relative to the system boundaries.

We therefore estimate, for each magnetosheath measurement, its relative radial distance to the magnetopause and bow shock, at the time at which it was performed. These relative radial distances are then used to re-position each measurement radially in between a standardized set of boundaries (Jelínek et al., 2012; Shue et al., 1998), keeping the same angular position. Knowing where the boundaries are at each time is impossible and must thus be somehow estimated. Here, the radial distance of the boundaries along the angular position of the spacecraft at time t is estimated from boundary models parametrized by IMF and solar wind properties previously obtained in the pairing procedure.

We have used gradient boosting regression models of the boundary radial positions from Michotte de Welle et al. 2022 (Michotte de Welle et al., 2022). These models have been trained to predict the radial position of the boundaries from thousands of crossings paired with IMF and solar wind conditions. These regression models result in smaller errors than analytical boundary models available in the literature, in particular close to the magnetopause with a Root Mean Square Error (RMSE) of 0.78 ± 0.03 Re for the magnetopause model and of 0.96 ± 0.06 Re for the bow shock model. A similar procedure is followed for magnetosphere measurements, which are radially re-positioned between $0R_e$ and the predicted radial position of the magnetopause at their timestamp. Only the magnetosphere measurements falling closer than $5R_e$ from the magnetopause are kept. Due to remaining inaccuracies in the boundary models, or possible mis-classification between near-Earth regions, some measurements classified as magnetosheath are found outside their predicted couple of boundaries and are thus discarded from the final subsets. After re-positioning, we obtain 44 and 54 million measurements in the magnetosheath and magnetosphere, respectively.

Figure 2 shows the magnetosphere and magnetosheath subsets once re-positioned between the standard boundaries.

2.5 Pseudo-GSM coordinate system

In theory, the GSM coordinate system is the most adapted for representing the maps we aim at producing. In practice, however, it is not convenient. Magnetopause crossings all together are spatially biased due to the specific spacecraft orbits. Even in large amounts, they do not result in a good spatial coverage of the whole dayside magnetopause in the GSM system as can be seen in figures 1 and 2. The situation becomes even worse when selecting only those for which their associated IMF and dipole conditions are nearby a specific configuration.

We therefore need to introduce various assumptions of symmetries of the system, to obtain a good spatial coverage. These symmetries, which are of different nature for the magnetosheath and magnetosphere data, are at the root of what we call here the *pseudo-GSM* (PSGM) coordinate system.

Regarding the magnetosphere, first, we assume the system is symmetric with respect to reversal of the dipole tilt angle. The number of points is thus doubled by duplicating each measurement i at position $(X_{GSM}, Y_{GSM}, Z_{GSM})$ with a magnetic field $(B_{xGSM}, B_{yGSM}, B_{zGSM})$, for a dipole tilt angle Ψ_{GSM} at a new position $(X_{GSM}, -Y_{GSM}, -Z_{GSM})$ with a magnetic field $(-B_{xGSM}, B_{yGSM}, B_{zGSM})$ and a dipole tilt $-\Psi_{GSM}$.

Then, regarding magnetosheath measurements, we assume the draping pattern only depends on the absolute value of the IMF cone angle. Said differently, we assume the draping geometry obtained when the IMF clock angle is, say, 90° is the same as the one obtained when it is due north 0° but only rotated by 90°. Another way to see it is that we consider that the IMF only drapes and slips around an axisymmetric magnetopause. Processes such as magnetic reconnection, which notably depend on the IMF clock angle, could, to some extent, break the symmetry, but are of negligible importance as a first approximation. This assumption was used successfully to reconstruct the magnetic draping pattern in Michotte de Welle et al. 2022 (Michotte de Welle et al., 2022).

In practice, as is represented in Fig. 3, magnetosheath measurements are first transformed from the GSM coordinate system into the Solar Wind Interplanetary (SWI) magnetic field coordinate system (Zhang et al., 2019). This coordinate system allows each point to fall in the "right" sector of a unique magnetosheath frame (i.e. quasi-parallel or quasi-perpendicular sides) with respect to its causal IMF. It is such that the X_{SWI} axis is anti-parallel to the solar wind velocity vector ($\mathbf{V}_{sw}$) and Y_{SWI} is along the direction of the IMF ($\mathbf{B}_{imf}$) component orthogonal to the X_{SWI} axis with Bx_{imf} always positive. Equations (**??**) give the unit vectors of the SWI basis for each magnetosheath measurements.

$$\begin{cases} \widehat{\mathbf{X}}_{\text{SWI}} &= -\mathbf{V}_{sw}/\|\mathbf{V}_{sw}\| \\ \widehat{\mathbf{Y}}_{\text{SWI}} &= \widehat{\mathbf{Z}}_{\text{SWI}} \times \widehat{\mathbf{X}}_{\text{SWI}} \\ \widehat{\mathbf{Z}}_{\text{SWI}} &= \left(\widehat{\mathbf{X}}_{\text{SWI}} \times \frac{Bx_{imf}}{|Bx_{imf}|}\mathbf{B}_{imf}\right) / \|\widehat{\mathbf{X}}_{\text{SWI}} \times \frac{Bx_{imf}}{|Bx_{imf}|}\mathbf{B}_{imf}\| \end{cases} \tag{1}$$

An immediate advantage of using this system and symmetry is that, two distinct measurements such as the red and green points on panels **A** and **B** of Fig. 3, contributing, at their location in GSM, to draping patterns associated with IMF clock angle 45° and −45°, respectively, will both contribute to the same draping pattern shown on panel **C**, thereby vastly improving the spatial coverage.

The number of measurements for absolute values of the IMF cone angle decreases sharply below 45° (Michotte de Welle et al., 2022). Therefore, we also assume the draping is symmetric with respect to the Y_{SWI} axis, and each magnetosheath measurement is duplicated with $Z_{SWI} \to -Z_{SWI}$ and $B_{zSWI} \to -B_{zSWI}$. Magnetosheath data projected in this symmetric SWI coordinate system cannot yet be used with magnetosphere

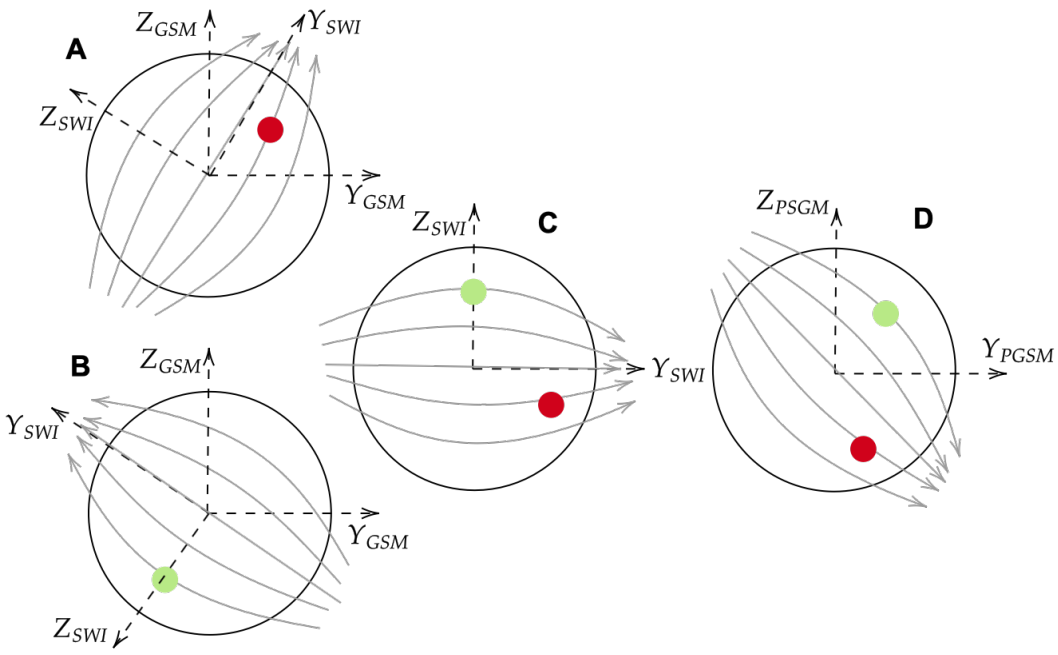

Figure 3. Schematic representation of the transformation from the GSM to the PGSM coordinate system. The black circles correspond to the intersection of the magnetopause surface with the YZ plane at $X = 0$. The solid black bent arrows represent the draped magnetic field. Dark red and light green points represent two distinct measurements, made for IMF clock angles 45° and −45° Panel A and B show the red and green points in the GSM coordinate system. Panel C represents the draped magnetic field in the SWI coordinate system. Panel D represents the draping in the PGSM system for an IMF clock angle of 120°

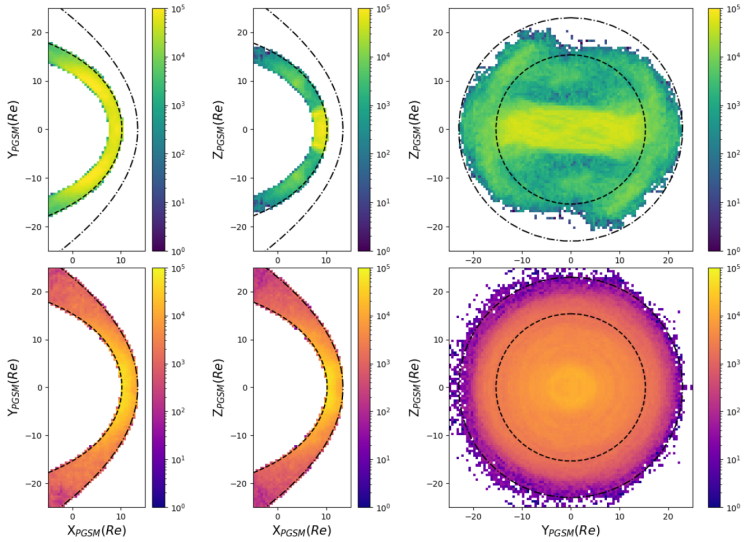

Figure 4. Distributions of magnetosphere (upper panels) and magnetosheath (lower panels) data point positions in the PGSM coordinate system, presented through color-coded bins indicating the number of points per bin. Format is the same as Fig. 1.

data to reconstruct magnetopause maps since in SWI, the draping pattern always looks as if in GSM, the IMF clock angle always was 90°, as represented on panel **C** of Fig. 3. To reconstruct a global distribution of a quantity for a specific IMF cone and clock angles, as if in GSM coordinates, a subset of the magnetosheath measurements within a specific range of IMF cone angles can be selected and then rotated around the X axis by an angle of $\Delta\theta_{cl} = \theta_{cl} - \pi/2$, where θ_{cl} is the desired IMF clock angle in radians. This transformation is represented as the transition from panel **C** to panel **D** of Fig. 3, where the draping is rotated to correspond to that of an IMF clock angle of 120°. The equations 2 and 3 provide the details for this rotation for the measurements' position and the magnetic field, respectively. It is performed with taking into account the sign (i.e. $\pm$) of the desired $B_{x_{imf}}$ component, positive for $B_{x_{imf}} > 0$ and negative for $B_{x_{imf}} < 0$.

After these transformations, magnetosphere and magnetosheath subsets can be used together in this PSGM coordinates, as if obtained in the GSM system. Data in this final form is represented in the various panels of Fig. 4.

$$\mathbf{X}_{\mathrm{MSH}} \begin{cases} X_{\mathrm{PGSM}} &= X_{\mathrm{SWI}} \\ Y_{\mathrm{PGSM}} &= \sqrt{Y_{\mathrm{SWI}}^2 + Z_{\mathrm{SWI}}^2}\,\sin(\tan^{-1}(\pm Y_{\mathrm{SWI}}/Z_{\mathrm{SWI}}) + \Delta\theta_{cl}) \\ Z_{\mathrm{PGSM}} &= \sqrt{Y_{\mathrm{SWI}}^2 + Z_{\mathrm{SWI}}^2}\,\cos(\tan^{-1}(\pm Y_{\mathrm{SWI}}/Z_{\mathrm{SWI}}) + \Delta\theta_{cl}) \end{cases} \quad \text{with} \quad \tan^{-1}\left(\frac{\pm Y_{\mathrm{SWI}}}{Z_{\mathrm{SWI}}}\right) \in [-\pi, \pi] \tag{2}$$

$$\mathbf{B}_{\mathrm{MSH}} \begin{cases} B_{x_{\mathrm{PGSM}}} &= \pm B_{x_{\mathrm{SWI}}} \\ B_{y_{\mathrm{PGSM}}} &= \sqrt{B_{y_{\mathrm{SWI}}}^2 + B_{z_{\mathrm{SWI}}}^2}\,\sin(\tan^{-1}(B_{y_{\mathrm{SWI}}}/(\pm B_{z_{\mathrm{SWI}}})) + \Delta\theta_{cl}) \\ B_{z_{\mathrm{PGSM}}} &= \sqrt{B_{y_{\mathrm{SWI}}}^2 + B_{z_{\mathrm{SWI}}}^2}\,\cos(\tan^{-1}(B_{y_{\mathrm{SWI}}}/(\pm B_{z_{\mathrm{SWI}}})) + \Delta\theta_{cl}) \end{cases} \quad \text{with} \quad \tan^{-1}\left(\frac{B_{y_{\mathrm{SWI}}}}{\pm B_{z_{\mathrm{SWI}}}}\right) \in [-\pi, \pi] \tag{3}$$

2.6 Global distributions at the magnetopause using in-situ measurements

The construction of a map for a specific IMF orientation and dipole tilt angle first consists in putting magnetosphere and magnetosheath data into the PGSM coordinate associated with these angles. Then, we select the subset of magnetosheath (resp. magnetosphere) data for which the IMF cone angle (resp. the dipole tilt angle) is at most 5° (resp 2.5°) away from the desired angle. At this point, we have a randomly scattered distribution of in-situ measurements in PGSM coordinates, from which we desire to draw a global and continuous spatial representation of a quantity at the magnetopause. This is done by using a K-Nearest Neighbors (kNN) algorithm (Pedregosa et al., 2011), which computes the distance-weighted average of the K closest measurements to nodes of a meshed magnetopause smooth surface model (Shue et al., 1998) parameterized with average solar wind and IMF conditions (i.e. dynamic pressure of 2nPa and $B_{z_{imf}} = 0$ nT). The value of K is typically chosen between 7500 and 10,000, depending on the size of the selected subset of data considered.

It is important to note that the maps we construct represent the variations of a given quantity on the magnetopause, as imposed by the magnetosheath and magnetosphere properties, excluding its local variations due to internal magnetopause processes. In a similar spirit as the magnetic shear angle maps often used to predict X-lines (Trattner et al., 2021), the current density we aim at mapping, is the one expected on the magnetopause from the draped and piled up IMF on one side, and the dipolar magnetospheric field on the other. We do not aim at producing a map of the measured current density resulting from processes internal to the magnetopause itself. The following paragraphs explain how we compute the magnetic shear angle, the current density and the potential reconnection rate on this mesh, using magnetosheath and magnetosphere quantities in the PGSM coordinate system.

2.6.1 Magnetic shear angle spatial distribution

The magnetic shear angle is determined by using the global distributions of the magnetic fields on both sides of the magnetopause. The kNN algorithm is used with data subsets selected based on a range of dipole tilt and IMF cone angles for the magnetosphere and the magnetosheath, respectively. Each magnetic field measurement, in the magnetosheath and magnetosphere, has a small component normal to the magnetopause surface used in our maps. Such a small normal component may be due to magnetic reconnection. But more probably, it arises from the local inconsistency between the smooth magnetopause surface we use for representation purposes, and the real magnetopause close to which measurements were made. For consistency with previous work, and because we aim at understanding how pristine magnetosheath and magnetosphere configurations could constrain reconnection at the magnetopause, we assume that the magnetic fields are tangential to the magnetopause surface. We thus remove from the magnetic field vectors obtained at each node of the meshed boundary surface, the small component locally normal to the surface. Finally, computing the line that maximizes the shear angle requires a smooth spatial distribution, so a gaussian filter with a standard deviation of about 2 Re is applied to both magnetic fields ($\mathbf{B}_{\mathrm{MSP}}$ and $\mathbf{B}_{\mathrm{MSH}}$) before calculating the magnetic shear angle with equation 4.

$$\alpha = \cos^{-1}\left(\frac{\mathbf{B}_{\mathrm{MSP}} \cdot \mathbf{B}_{\mathrm{MSH}}}{\|\mathbf{B}_{\mathrm{MSP}}\|\|\mathbf{B}_{\mathrm{MSH}}\|}\right) \tag{4}$$

2.6.2 Current density spatial distribution

The global distribution of the current density $\mathbf{J}$ is calculated using the Ampere equation (eq. 5) and the magnetic fields at the magnetopause determined in the section 2.6.1. The calculation is done in a basis with one unit vector, $\widehat{\mathbf{N}}$, along the local normal to the

magnetopause surface, and the other two unit vectors, $\widehat{\mathbf{L}}$ and $\widehat{\mathbf{M}}$, chosen such that the first one is along the magnetospheric magnetic field and the second completes the basis. Contrary to the shear angle, computing the current density requires making an assumption about the thickness of the magnetopause (d_{mp}) The current density we compute here is the one associated with the large scale variation of the magnetic field across the magnetopause from the draped IMF to the dipolar magnetospheric field. The magnetopause often has an internal structure composed of several thinner sub layers that we do not take into account here. Observations also indicate that the magnetopause is thinner in the subsolar region ($\sim 700\ km$) than it is in the flanks ($\sim 900\ km$) (Haaland et al., 2020). This weak large scale variation of the magnetopause thickness will act to increase the current density in the dayside region. While interesting, we consider this effect to be of second order importance compared to the variation of the current induced by the tangential variation of the shear angle and magnetic jump and adding a model of the thickness variation would probably add more uncertainty to the outcome of the study than new findings. We thus use an average and uniform value of $d_{mp} = 800\ km$ as a compromise between above values. Each magnetic field measurement on the magnetosheath side is normalized by the amplitude of the IMF magnetic field to which it is paired. Then, the dimensionless magnetic field predicted by the kNN is multiplied by 5 nT, which close to the average IMF amplitude. Current density maps are thus obtained in nA/m^2.

$$\mathbf{J} = \frac{\nabla \times \mathbf{B}}{\mu_0} = J_l\widehat{\mathbf{L}} + J_m\widehat{\mathbf{M}} \quad \text{with} \quad \begin{cases} \widehat{\mathbf{L}} & = \mathbf{B}_{\mathrm{MSP}}/\|\mathbf{B}_{\mathrm{MSP}}\| \\ \widehat{\mathbf{M}} & = \widehat{\mathbf{N}} \times \widehat{\mathbf{L}} \end{cases} \quad \text{and} \quad \begin{cases} J_l & \approx \frac{-(B_{m_{\mathrm{MSH}}} - B_{m_{\mathrm{MSP}}})}{d_{\mathrm{mp}}\mu_0} \\ J_m & \approx \frac{B_{l_{\mathrm{MSH}}} - B_{l_{\mathrm{MSP}}}}{d_{\mathrm{mp}}\mu_0} \end{cases} \tag{5}$$

2.6.3 Reconnection rate spatial distribution

The potential reconnection rate (Eq. 6) is determined using the Cassak-Shay formula ((Cassak & Shay, 2007)) for asymmetric upstream conditions. Additionally to the magnetic fields, it requires the global distribution of the particles density (ρ_{MSP} and ρ_{MSH}) on both side of the magnetopause. These densities are obtained using kNNs on each node of the meshed magnetopause and then smoothed with a gaussian filter (see section 2.6.1). The Cassak-Shay scaling law was developed for anti-parallel magnetic fields. However, in general, the magnetic fields at the magnetopause are not coplanar. Therefore, the reconnecting components must be determined to compute the reconnection rate. In this study, they are determined so that the Cassak-Shay formula is maximized, i.e. for an angle ξ between the X-line and the magnetospheric magnetic field such that the reconnection rate satisfies $\partial R/\partial\xi = 0$ (Komar et al., 2015). In equation 6, the aspect ratio δ/Δ is taken equal to 0.1 (Y.-H. Liu et al., 2017), α is the magnetic shear angle (Eq 4) used with the angle ξ to determine the reconnected components of the magnetic fields on each side of the magnetopause.

$$R = \frac{2\delta}{\Delta} \frac{\left(\|\mathbf{B}_{\mathrm{MSP}}\| \sin(\xi) \|\mathbf{B}_{\mathrm{MSH}}\| \sin(\alpha - \xi)\right)^{3/2}}{\sqrt{\mu_0(\|\mathbf{B}_{\mathrm{MSP}}\| \sin(\xi) + \|\mathbf{B}_{\mathrm{MSH}}\| \sin(\alpha - \xi))(\rho_{\mathrm{MSH}}\|\mathbf{B}_{\mathrm{MSP}}\| \sin(\xi) + \rho_{\mathrm{MSP}}\|\mathbf{B}_{\mathrm{MSH}}\| \sin(\alpha - \xi))}} \tag{6}$$

2.7 Modeled magnetic shear spatial distribution

Magnetic shear maps are also computed with modeled magnetic fields. In this case, the magnetic field on the magnetosphere side of the magnetopause is calculated by combining the International Geomagnetic Reference Field (IGRF) and the Tsyganenko & Stern 1996 (Tsyganenko & Stern, 1996) models, hereafter noted as T96. This model predicts the presence in the dayside of open magnetic field lines, resulting in a magnetic field

non-tangential to the magnetopause and therefore in a magnetic shear out of the boundary plane. To ensure that magnetic field lines are closed, the IMF B_y and B_z components required in the T96 model are set to zero. The magnetopause location is defined by the Sibeck et al. model (S91) (Sibeck et al., 1991) in the T96 model. Therefore, in order to determine the magnetospheric magnetic field at the magnetopause, the T96 model is used on a meshed surface obtained with the S91 model.

Regarding the magnetosheath side of the magnetopause, the draped magnetic field is obtained using the KF94. It is defined by a magnetic potential valid between parabolic and confocal boundaries obtained with equation 7 (Romashets & Vandas, 2019), with θ the elevation angle relative to the X axis, x_0 and x_1 correspond to the standoff distances of the magnetopause and shock respectively. These standoff distances are obtained using the S91 magnetopause and the Jelinek et al. ((Jelínek et al., 2012)) bow shock models.

$$\sin^2(\theta)R_{mp,bs}^2 + 4(x_{0,1} - x_0/2)\cos(\theta)R_{mp,bs} - 4(x_{0,1} - x_0/2)x_{0,1} = 0 \tag{7}$$

The parabolic approximation of the magnetopause model creates a slightly different shape than that used for the magnetospheric magnetic field. To align the fields on both sides of the magnetopause, the magnetosheath magnetic field is estimated where the normal to the S91 surface intersects its parabolic approximation.

2.8 Computing X-lines from local maxima

In this section, we explain how we compute the position of an X-line following the global approach, i.e. by finding the line that maximizes the considered quantity given its spatial distribution on the magnetopause. In all cases, since this study focuses on dayside reconnection, we decide not to draw lines when the IMF is oriented too northward (clock angles below 25°).

2.8.1 Maximum magnetic shear lines

The component reconnection part of the Maximum Magnetic Shear Line (MSL) is obtained by integrating the magnetic shear gradient from the saddle point between the two anti-parallel branches. Following the gradient from the saddle point between two maxima allows to obtain the shortest line that maximizes a quantity. A saddle point is an extremum point that can be identified by the presence of eigenvalues of the Hessian matrix with opposite signs, indicating opposite signs of curvatures. At the saddle point, where the gradient is zero, the initial step of the integration follows the eigenvector corresponding to the largest eigenvalue of the Hessian matrix which gives the direction of the local maximum curvature. The next integrating steps follow the magnetic shear gradient until the component reconnection part of the MSL reaches the anti-parallel regions, where the integration stops since the gradient there is zero. The anti-parallel branches are obtained using a local maxima detection algorithm (van der Walt et al., 2014) to find the points along anti-parallel magnetic shear regions. These points are interpolated into the two anti-parallel branches, which are then added to the component reconnection part of the MSL. The distribution of the shear angle for IMF clock angle of 0° and 180°, are such that no MSL can be constructed in the dayside region.

2.8.2 Maximum current density and reconnection rate lines

Obtaining the Maximum Current Density Lines (MCLs) and Maximum Reconnection Rate Lines (MRLs) is a more complex process than for MSLs, because these distributions reveal one or more saddle points and/or maxima. There is therefore no unique

maximum path on such complex surfaces and a decision is needed about the starting integration point.

Our driving idea is to compute X-lines that explore the dayside magnetopause, i.e. that pass equatorwards of the cusps, a reasonable choice considering this is were the IMF first touches the magnetopause.

Whenever the current and reconnection rate maps show a global maximum around the subsolar region, which typically occur when the IMF has a southward component, we follow the line departing from that maximum along the local eigenvector of the Hessian matrix that corresponds to the smallest negative eigenvalue (see section 2.8.1). This technique is for instance used in Figure 11h, i, and j.

In northward IMF conditions, the current and reconnection rate maps typically show two local and high maxima located poleward of the cusps. The global line is thus obtained by following the gradient up to the poleward maxima from the dayside saddle points. The possible existence of a (smaller) local maximum in the subsolar region, indicates one or more saddle points in the dayside, in which case several line portions are computed and eventually merged into a single global one. Figure 11g shows an example of such an X-line.

3 Comparison of observed and modeled magnetic shear spatial distributions

This section aims at comparing magnetic shear maps produced using magnetic field models for the magnetosheath (KF94) and the magnetosphere (T96), with those made using only in-situ measurements. It is important to evaluate the validity of the modeled shear maps, as they are often used to predict the location of magnetic reconnection and other phenomena at the magnetopause (Trattner et al., 2017; Petrinec et al., 2022; Sun et al., 2022). The magnetic field draping in the magnetosheath can be classified into three regimes as a function of the IMF cone angle : large (($|\theta_{co}| \geq 45° \pm 5°$), intermediate ($45° \pm 5° \geq |\theta_{co}| \geq 12.5° \pm 2.5°$), and low ($|\theta_{co}| \leq 12.5° \pm 2.5°$) values, as shown in Michotte de Welle et al. 2022 (Michotte de Welle et al., 2022). Correspondingly, this section will be divided into three subsections. Note that the maps obtained studied in these subsections will reproduce published cases, when available, in order to show the validity of our method (see section 2.7).

3.1 Large IMF cone angles

The large IMF cone angle regime, as defined in Michotte de Welle et al. 2022 ((Michotte de Welle et al., 2022)), corresponds to orientations within $|\theta_{co}| \geq 45° \pm 5°$, which represents about 70% of the IMF orientations measured at 1 AU. Figure 5 shows maps of the magnetic shear angle at the magnetopause as viewed from the Sun assuming steady state. The Figure 5.**b** reproduces the modeled magnetic shear map of Trattner et al. 2021(Trattner et al., 2021) (Fig.13) on the 20 September 1997 at 07:34 UT with a dipole tilt of -6.6°, an IMF cone angle of -80.7°, and an IMF clock angle of 130°. The magnetic shear map in Figure 5.**a** is obtained from in-situ data only. The magnetic field on the magnetosheath side of the magnetopause is made for the subset of the data associated with an IMF cone angle falling within the range $76° \leq |\theta_{co}| \leq 86°$, and with an IMF clock angle set to 130° in the PGSM coordinate system. The in-situ measurements on the magnetospheric side are selected for an associated dipole tilt of ψ = - 6.6°±2.5°.

The modeled shear map (Fig. 5.**b**) exhibits a high similarity with the one obtained using in-situ data (Fig. 5.**a**). This outcome could be anticipated as the KF94 magnetic draping is very similar to the observed one for large IMF cone angles (Michotte de Welle et al., 2022). The shape of the anti-parallel areas is the most noticeable difference be-

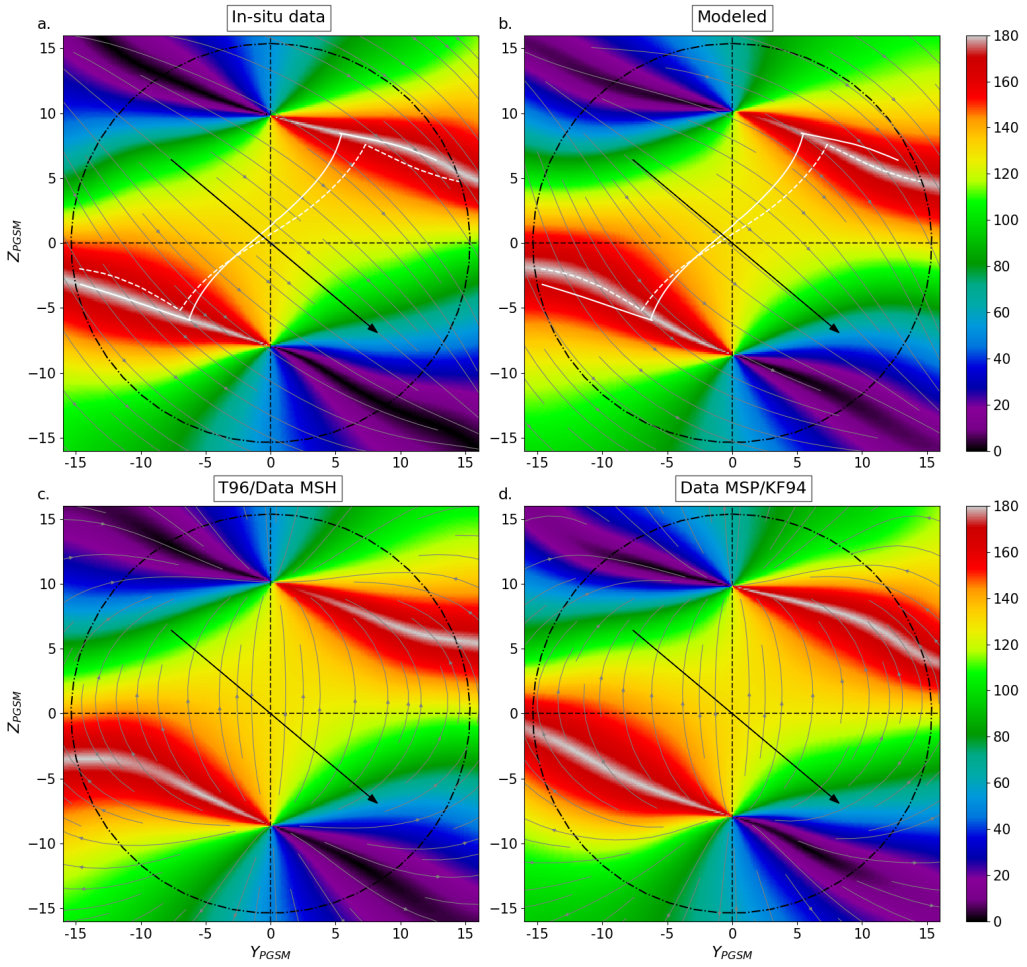

Figure 5. Magnetic shear maps at large IMF cone angle. Panels **a** and **b** correspond to the magnetic shear angle maps using only in-situ measurements and magnetic field models (Tsyganenko & Stern, 1996; Kobel & Fluckiger, 1994), respectively. The magnetic shear map on panel **b** correspond to the one presented in Trattner et al. 2021(Trattner et al., 2021) (Fig.13) on 20 September 1997 at 07:34 UT. The map in panel **c** is made with the T96 model and the magnetosheath in-situ measurements. The map in panel **d** is made with the magnetosphere in-situ measurements and the KF94 model. The subset of in-situ magnetosheath measurements used in panels **a** and **c** is $76^\circ \leq |\theta_{co}| \leq 86^\circ$ and turned to an IMF clock angle of 130°. The subset of in-situ magnetosphere measurements used in panels **a** and **d** is $|\psi| = 6.6^\circ \pm 2.5^\circ$. The value of dipole tilt of modeled magnetospheric magnetic field ((Tsyganenko & Stern, 1996)) used in the panels **b** and **c** is -6.6°. The modeled magnetosheath magnetic field ((Kobel & Fluckiger, 1994)) in the panels **b** and **d** is made with $(Bx_{imf}, By_{imf}, Bz_{imf})$=(-0.7,3.8,-3.2). The grey arrowed lines in the panels **a** and **b** (resp. **c** and **d**) represent magnetic field lines of the observed and modeled magnetosheath (resp. magnetosphere), respectively. The solid and dashed white lines maximize the observed and modeled magnetic shear, respectively. The black arrows correspond to IMF orientation in the (YZ) plane. The terminator is represented by the dashed circle.

tween the two magnetic shear maps (Fig. 5.**a**, **b**). In the map made with magnetic field models, they are bending to become nearly parallel to the equator. In contrast, in the map made in-situ measurements, they remain almost straight. To investigate the origin of this difference, we computed magnetic shear maps made using in-situ measurements on one side of the magnetopause and a magnetic field model (either T96 or KF94) on the other side (Fig. 5 **c** and **d**). As the magnetic shear map using in-situ magnetospheric measurements and the KF94 model (Fig. 5.**d**) displays anti-parallel areas similar to the observed map, while the T96/magnetosheath data map (Fig. 5.**c**) shows patterns comparable to figure 5**b**, we conclude that the discrepancy arises from the magnetospheric magnetic field. A possible explanation for these differences is that the T96 model uses a magnetopause model (S91) independent of the dipole tilt angle, whereas the shape of the magnetopause is actually affected by it (Lin et al., 2010; Z. Q. Liu et al., 2015; Nguyen et al., 2022b). Since the T96 model magnetic field must remain tangent to the magnetopause surface, this could result in a slight difference in curvature between the modeled (Fig. 5.**c**) and observed (Fig. 5.**d**) magnetic field lines. Additionally, a part of these discrepancies may arise from the slight difference of shape between the magnetopause models used in the observed (Shue et al., 1998) and modeled (Sibeck et al., 1991) maps. Further investigation is required but is outside the scope of this study.

The Maximum Shear Line (MSL), which maximizes locally the magnetic shear angle on the magnetopause surface, is often used to predict the location of the X-line (Trattner et al., 2007). On average, observed and modeled MSLs (Fig. 5.**a** and **b**) are about 1 Re apart. It should be noted that the component reconnection part of the modeled MSL is more inclined toward the equator than the one from observations (Fig. 5.**a** and **b**). And while the maps obtained with the T96/KF94 models in the large IMF cone angle regime provide a reliable qualitative estimate of the magnetic shear at the magnetopause, we will see later (section 4.1.1) that the discrepancy in the orientation of the MSL actually shows a significant difference in term of its dependence on the IMF direction, between the modeled and observed maps.

3.2 Intermediate IMF cone angle

Figure 6 shows an observed (panel **c**) and modeled (panel **d**) shear map for an IMF cone angle in the intermediate regime (i.e. $45^\circ \pm 5^\circ \geq |\theta_{co}| \geq 12.5^\circ \pm 2.5^\circ$), which represents about 28% of the IMF. Figure 6.**d** reproduces the modeled magnetic shear map of Trattner et al. 2012(Trattner et al., 2012b) (Fig.4) on 22 Mars 1996 at 02:40 UT with a dipole tilt of -8.2°, an IMF cone angle of 18.5°, and an IMF clock angle of 99°. The observed magnetic shear map in Figure 6.**c** is made with the subset of the magnetosheath measurements for which the IMF cone angle lies within $13.5^\circ \leq |\theta_{co}| \leq 23^\circ$ and an IMF clock angle set to 99° in the PGSM coordinate system. The in-situ measurements on the magnetospheric side are selected for an associated dipole tilt of ψ = -8.2°±2.5°.

In the modeled shear map (Fig. 6**d**), parallel and anti-parallel magnetic shear areas join on the dayside of the quasi-parallel magnetopause. This pattern results from the convergence (or divergence, depending on the sign of $B_{x_{imf}}$) of the magnetosheath field lines predicted by the KF94 model towards a topological singularity ($Y_{PGSM} \approx 7.5$ Re and $Z_{PGSM} \approx -1.5$ Re) aligned with the parallel bow shock, visible in panel **b**. In contrast, in the observed shear map (Fig. 6**ca**), the parallel and anti-parallel magnetic shear areas do not connect on the quasi-parallel magnetopause, but instead extend towards the nightside. This difference results from the absence of the aforementioned singularity in the observed magnetic field draping for such an IMF cone angle as visible on panel **a** and discussed in Michotte de Welle et al. 2022 (Michotte de Welle et al., 2022). As seen with the solid and dashed white lines, throughout most of the dayside, the observed and modeled MSLs are approximately 2 Re apart, but this distance significantly increases up to around 8 Re on the quasi-parallel side of the magnetopause at dusk.

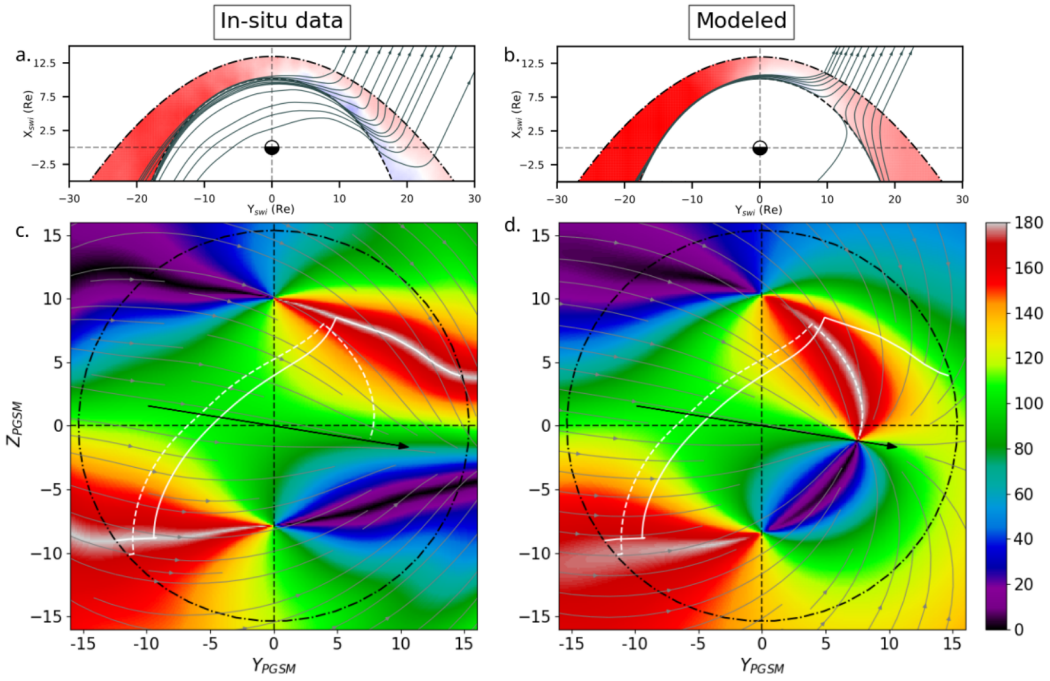

Figure 6. Magnetic draping and magnetopause magnetic shear maps at intermediate IMF cone angle. Subsets $13.5^\circ \leq |\theta_{co}| \leq 23^\circ$ and $|\psi| = 8.2^\circ \pm 2.5^\circ$. Panel **a** and **b** represent, in the SWI coordinate system, the color coded B_x component of the magnetic field and magnetic field lines (solid black lines) reconstructed from observations (panel **a**) and predicted by the KF94 models (panel **b**), from Michotte de Welle et al. 2022 (Michotte de Welle et al., 2022). Panels **c** and **d** correspond to the magnetic shear angle maps made using only in-situ measurements and magnetic field models ((Tsyganenko & Stern, 1996; Kobel & Fluckiger, 1994)), respectively. The magnetic shear map on panel **b** correspond to the one presented in Trattner et al. 2021(Trattner et al., 2012b) (Fig.4) on22 Mars 1996 at 02:40 UT. The grey arrowed lines represent in the panels **a** and **b** represent magnetic field lines of the observed and modeled magnetosheath draping, respectively. The solid and dashed white lines maximize the observed and modeled magnetic shear (MSL), respectively. The black arrows correspond to IMF orientation in the (YZ) plane.

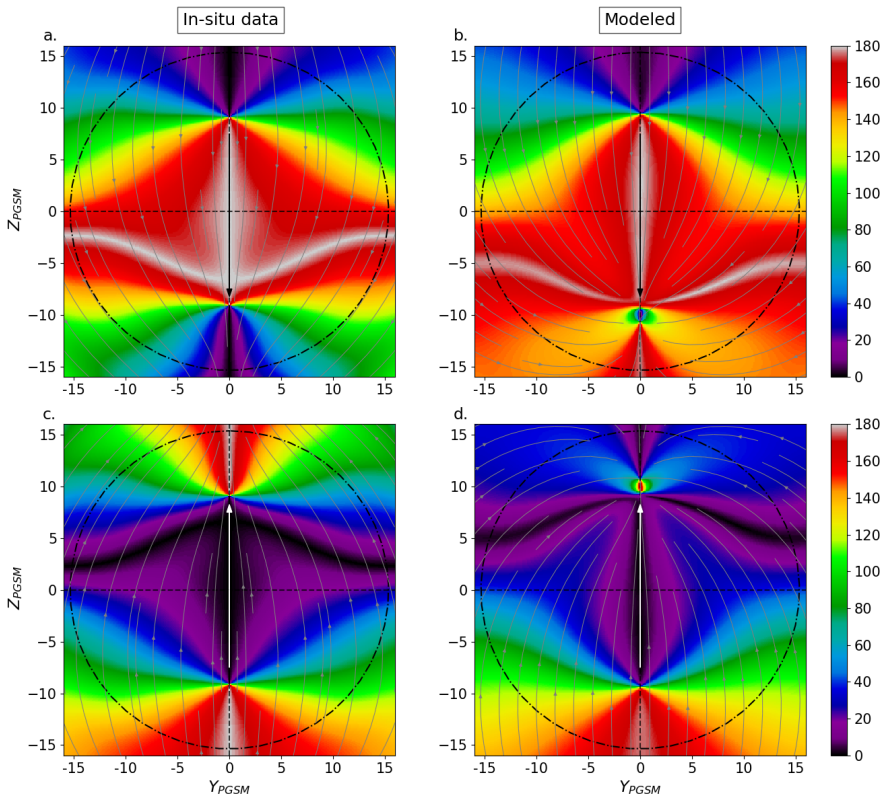

Figure 7. Magnetic shear maps at intermediate IMF cone angle. Subsets θ_{co} =25°±5° and $|\psi|$ = 0°±2.5° with θ_{cl} =180° (Panel a and b) and θ_{cl} =0° (Panel c and d). The legend is the same as Figure 6.

The absence of a divergent pattern in the observed magnetosheath draping leads to unexpected effects when the region of the magnetosheath behind the quasi-parallel shocks is located on one of the lobes, as shown in Figure 7 for an IMF clock angle of 180° (panels **a**,**b**) or of 0° (panels **c**,**d**). For an IMF clock angle of 180°, both observed and modeled maps exhibit the majority of the dayside magnetopause at high magnetic shear, with an anti-parallel area in the southern hemisphere due to asymmetry in the magnetosheath draping. However, the modeled map (Fig. 7 **b**) predicts that most of the southern lobe has a high magnetic shear because the divergent pattern predicted by the KF94 model is located equatorward of the southern cusp. In contrast, without this singularity, the observed map (Fig. 7 **a**) displays low shear angles across the entire south lobe. The situation for an IMF clock angle of 0° is similar but reversed, with the observed map (Fig. 7 **c**) showing high magnetic shear in both lobes, while only in the southern lobe for the modeled map (Fig. 7 **d**). An important conclusion from this comparison is that if only considering the magnetic shear for determining the location of magnetic reconnection, both lobes are equally important in observations while they are significantly different in the modeled map.

In general, the magnetic shear maps derived from the T96/KF94 models do not provide a reliable estimate of the observed shear angle at the magnetopause in the intermediate IMF cone angle regime.

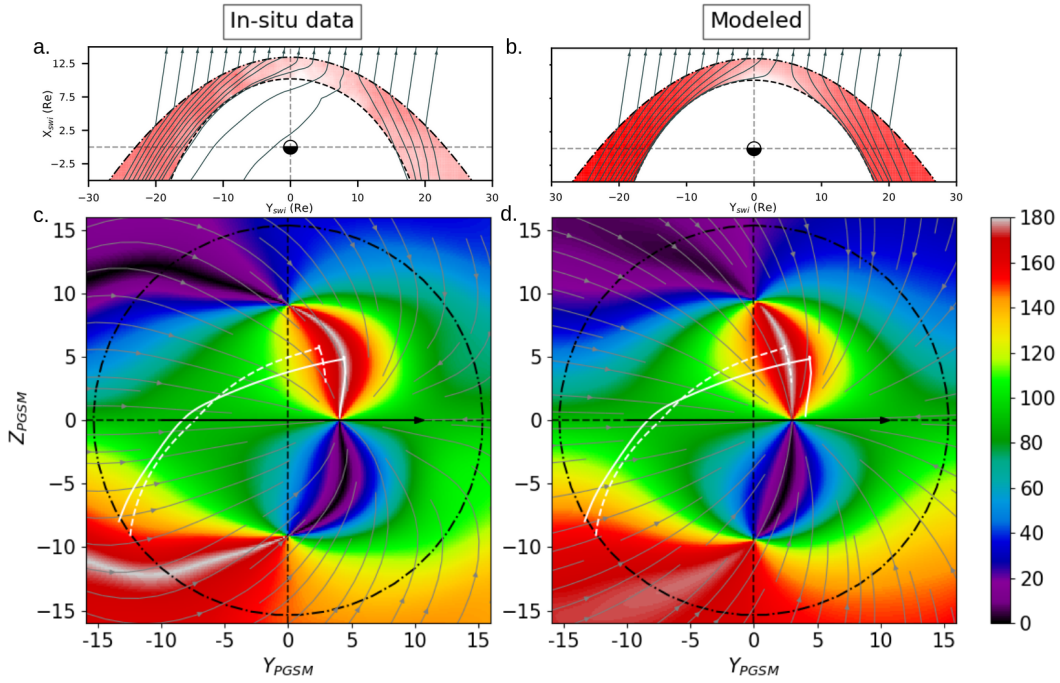

Figure 8. Magnetic draping and magnetic shear maps at low IMF cone angle. Subsets $|\theta_{co}| \leq 12.5°$ and $|\psi| = 0°\pm2.5°$ with θ_{cl} =90°. The legend is the same as Figure 6.

3.3 Low IMF cone angle

The low IMF cone angle regime (i.e $|\theta_{co}| \leq 12.5°\pm2.5°$) represents less than 2% of the IMF data. The maps in Fig. 8 display the magnetic shear for a due east IMF (i.e. $\theta_{cl} = 90°$) and a dipole tilt of 0° in the case of low IMF cone angle. The observed map (Fig. 8.**c**) is made using magnetosheath measurements within $|\theta_{co}| \leq 12.5°$ and a dipole tilt angle of $\psi = 0°\pm2.5°$ for the magnetosphere side. Since we did not find in the literature a case of a modeled magnetic shear map at a low IMF cone angle, the one of Figure 8.**d** was made for an IMF cone angle of 8.3°, corresponding to the average IMF cone angle for the selected subset of magnetosheath measurements.

The two maps generally agree, as both the modeled and observed magnetosheath magnetic draping display a divergent pattern (Michotte de Welle et al., 2022) and visible on panels **a** and **b** or Fig. 8, connecting the parallel and anti-parallel areas on the dayside magnetopause. However, in the observed map (Fig. 8c), these areas have a slightly rounder shape on the quasi-parallel side ($Y_{PGSM} \geq 0$) and are located at lower latitudes on the quasi-perpendicular side ($Y_{PGSM} \leq 0$) of the magnetopause than in the modeled map (Fig. 8d). These differences arise from subtle discrepancies between the modeled and observed magnetic fields in the magnetosheath. In reality, the field lines on the quasi-parallel side remain connected to their quasi-perpendicular counterparts because they are frozen in the magnetosheath plasma flow (Michotte de Welle et al., 2022). In contrast, this effect is not seen in the field lines predicted by the KF94 model, which leads to the shape of the magnetic field lines in Figure 8b,d, that tends to be less curved toward the $Y_{PGSM} < 0$ side than in the observed draping (Figure 8a,c).

On average, the MSLs are approximately 1 Re apart and located slightly more towards the anti-parallel regions. As in the large IMF cone angle regime, the modeled shear maps can provide a relatively good estimate of the magnetic shear angle at the magnetopause in the low IMF cone angle regime.

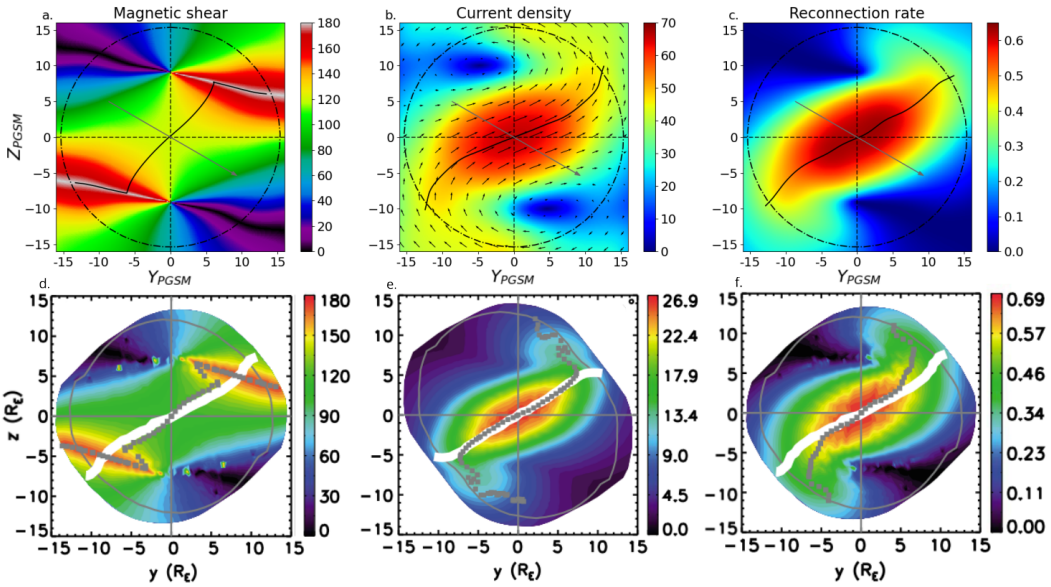

Figure 9. Panels a, b, and c show the global distributions of magnetic shear, current density (nA/m^2), and reconnection rate (mV/m), respectively, obtained from in-situ measurements for IMF cone angles in the range of $80° \leq |\theta_{co}| \leq 90°$, a dipole tilt angles of $\psi = 0° \pm 2.5°$, and an IMF clock angle of 120°. The black lines maximize the quantities represented in each panel. The gray arrows correspond to IMF orientation in the (YZ) plane. The terminator is represented by the dashed circle. Panels d, e, and f show the corresponding quantities obtained from a global MHD simulation in the study of Komar et al. 2015 (Komar et al., 2015) for similar IMF and dipole tilt orientations. The dotted gray line maximize the quantities and the white line correspond to the separator.

4 Global distribution of the magnetic shear, current density, and reconnection rate

Although the orientation of the magnetic fields on both sides of the magnetopause, as studied in the previous section, plays a crucial role in magnetic reconnection, other quantities are also important in this process, among which in particular the current density (Alexeev et al., 1998) and the reconnection electric field (Borovsky, 2013), etc. However, knowledge of their global distribution at the magnetopause comes only from modeling, usually numerical. In this study, in addition to the magnetic shear, we also obtained the current density and the Cassak-Shay asymmetric reconnection rate from an observational standpoint. In this section, we will first compare the global distribution of these quantities obtained with in-situ measurements with those obtained in published MHD simulation studies. Then, in the following subsections, we examine the variations of these quantities with respect to IMF orientation and dipole tilt angle.

Figure 9 shows the magnetic shear, current density, and reconnection rate at the magnetopause using in-situ measurements in panels a to c, respectively. These maps are made using measurements with IMF cone angles in the range of $80° \leq |\theta_{co}| \leq 90°$ and a dipole tilt angle of $\psi = 0° \pm 2.5°$. Panels d to f show the corresponding quantities obtained from a global MHD simulation in the study of Komar et al. 2015 ((Komar et al., 2015)). For all these maps the IMF clock angle has a value of 120°.

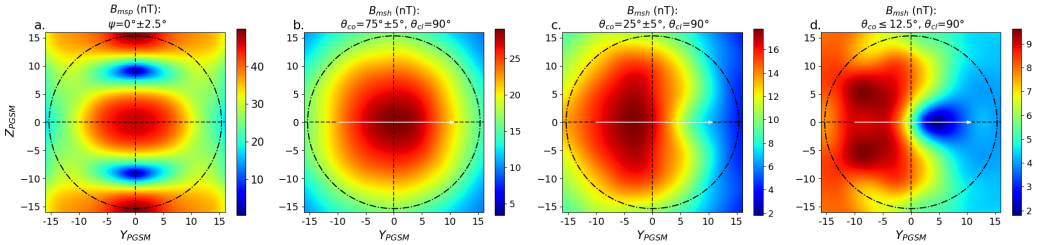

Figure 10. Amplitude of the magnetic fields at the surface of the magnetopause. Panel a shows the distribution of the magnetospheric magnetic field strength for a dipole tilt angle of ψ = 0°±2.5°. Panels b, c, and d show the amplitude of the magnetosheath magnetic field for large ($70° \leq |\theta_{co}| \leq 80°$), intermediate ($20° \leq |\theta_{co}| \leq 30°$), and small ($|\theta_{co}| \leq 12.5°$) IMF cone angle and an IMF clock angle of 90°, respectively.

The observed magnetic shear angle pattern (Fig. 9.a) closely resembles the one obtained in the global MHD simulation of Komar et al. 2015 (Komar et al., 2015) (Fig. 9.d). Interestingly, the MHD shear map, with an IMF orientation close to that in Figure 5, displays straight anti-parallel areas, consistent with observations from section 3.1. The observed MSL is consistent with the one obtained in the MHD simulation.

Figure 9.b shows a map of the current density at the magnetopause, where the direction of the current, indicated by black arrows, aligns with expectations for the given IMF orientation. The amplitude of the current density is maximum in the subsolar region, where the amplitude of the magnetic field magnitude on each side of the magnetopause (Fig. 10a and 10b) and the magnetic shear angle are highest. This amplitude remains large in both lobes due to the large differences in magnetic field strength between the magnetosphere and the magnetosheath. Finally, the current density amplitude is low in regions where the magnetic shear and the differences of strengths between the magnetic fields are small. The observed current density pattern remains consistent with MHD simulations (not shown) across different IMF orientations and dipole tilt angles found in published studies (Komar et al., 2015; Souza et al., 2017). The MHD current density amplitude, being of the same order of magnitude, is consistent with the observed map. The difference of amplitude between the two maps may arise from the resistivity set in the global simulation, which significantly impacts current density values (Glocer et al., 2016). In addition, if the orientation of the IMF is similar between the simulation and the measurements, it is not the case of other physical parameters that could influence the thickness of the magnetopause, which is assumed to be constant (800 km) in the observed map, but also the magnetic pileup, etc. The observed current density amplitude is remarkably consistent with studies using in-situ measurement. For instance, recent studies found median values of 62.1±1.5 nA/m^2 for the dayside and about 47±3.2 nA/m^2 for the flanks (Haaland et al., 2020); a current density distribution mostly between 10 nA/m^2 and 150 nA/m^2 (Lukin et al., 2020); and a median amplitude of the current density in the dayside magnetopause of 67.7±5.6 nA/m^2 (Beedle et al., 2022). It is worth noting that Figure 9.b represents the macroscopic current density at the magnetopause, but locally, the current can be highly inhomogeneous and exhibit stronger amplitudes. The Maximum Current density Line (MCL) that maximizes the current density is consistent with the one determined in the MHD simulation.

The reconnection rate in Figure 9c shows a pattern and amplitude very similar to that of the global MHD simulation of Komar et al. 2015 (Fig. 9.f). The highest values of the reconnection rate are in the subsolar region, where the high values of the magnetic pileup in the magnetosheath coincide with large magnetic shear (Fig. 9a). The lowest

reconnection rate values are found in regions of low magnetic shear, because the reconnected components of the magnetic fields would be extremely small. However, unlike the current density, a large difference in magnetic field amplitude between the magnetosphere and the magnetosheath (Fig. 10a and b) does not increase the rate. As a result, the reconnection rate at high latitudes experiences a rapid decline due to the decrease of the magnetic pileup in the magnetosheath. The similarity of the global pattern of the reconnection rate to MHD simulations remains consistent (not shown) across different IMF orientations and dipole tilt angles found in Komar et al. 2015 ((Komar et al., 2015)). The Maximum Rate Line (MRL) obtained from in-situ measurements appears straighter and more tilted toward the equator compared to that in Figure 9, yet remains consistent with it. In line with the observations made by Komar et al. (2015) for southward IMF, incorporating velocity shear (not shown) into the calculations of the reconnection rate (Cassak & Otto, 2011) has a negligible impact on its magnitude. Indeed, the correction is about one to two orders of magnitude smaller compared to the reconnection rate without velocity shear.

Overall, the global distribution of magnetic shear, current density, and reconnection rate obtained using only in-situ measurements agrees with numerical simulations.

4.1 Dependence on the IMF clock angle

We will now investigate the influence of the IMF clock angle on the distribution of the magnetic shear, the current density, and the reconnection rate on the magnetopause. This subsection is divided into three parts, corresponding to the different draping regimes, similar to the section 3.

4.1.1 Large IMF cone angle

Figure 11 shows the magnetic shear (panels a to e), the current density (panels f to j), and the reconnection rate (panels k to o) for a large IMF cone angle ($70° \leq |\theta_{co}| \leq 80°$) for a dipole tilt of 0° ($|\psi| = 0° \pm 2.5°$) as a function of the IMF clock angle (0°, 45°, 90°, 135°, and 180°).

For an IMF clock angle of 0° (Fig. 11a), the magnetic shear is anti-parallel in both lobes, with most of the dayside magnetopause exhibiting low shear angle values. As the IMF shifts southward (Fig. 11b,c,d), the magnetic shear angle on the dayside increases, with the anti-parallel (resp. parallel) shear regions moving closer to (resp. further from) the equator. Surprisingly, while the anti-parallel portion of the MSLs gets closer to the equator axis as the IMF clock angle increases, the global orientation of the component reconnection part of the lines appears to remain constant. In fact, when plotted together (Fig. 12.a), most of the component reconnection part of these MSLs overlap and remain close at high latitudes. This behavior has already been observed in a global MHD simulation study (Komar et al., 2015), which also found that the MSLs have a fixed orientation at the subsolar magnetopause and do not rotate for the different IMF clock angles. In contrast, the slopes of the modeled MSLs (Fig. 12.b) decrease with increasing IMF clock angle, resulting in a distance of about 5 Re at high latitude between the southernmost and northernmost lines. Further investigation revealed that the independence of the observed MSLs to the IMF clock angle is due to the magnetosheath magnetic field lines being less curved than those predicted by the KF94 model. This would result in a flatter gradient of the observed magnetic shear map than that produced by the models. Therefore, the component reconnection portion of the observed MSLs, following this gradient, would pass at roughly the same location in the component reconnection region and separate at higher latitudes where the magnetosheath field lines are more curved. The curvature differences between the modeled and observed draping could be explained by magnetic reconnection which affects the bending of the field lines by altering the global magnetosheath plasma flow. This effect would be observable only in in-situ measurements

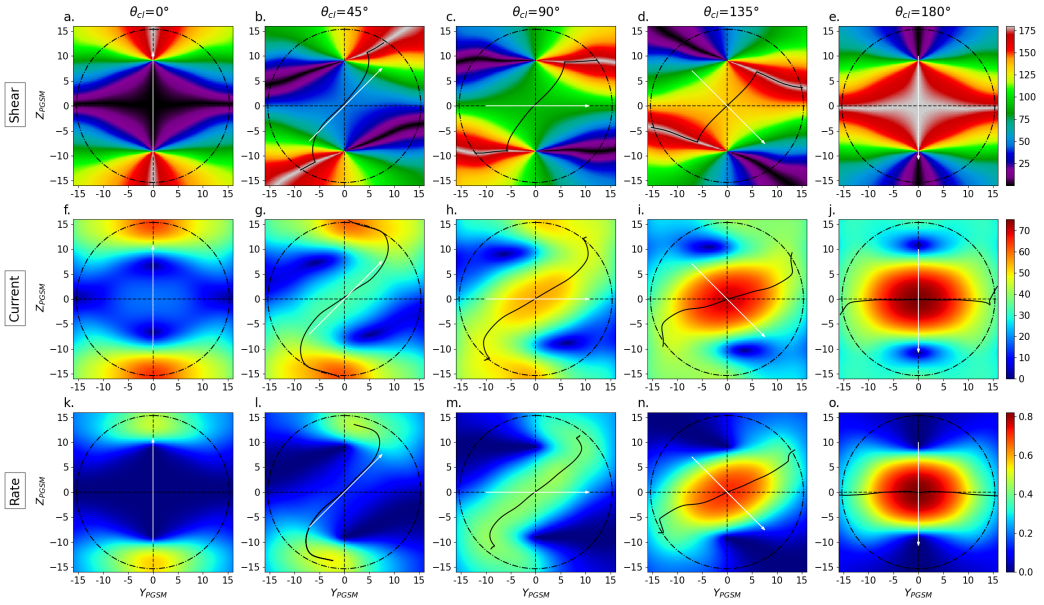

Figure 11. Global distributions of magnetic shear, current density, and reconnection rate at the surface of the magnetopause at Large IMF cone angles. Subsets of the measurement for IMF cone angles in the range $70° \leq |\theta_{co}| \leq 80°$ and dipole tilt angles of $|\psi| = 0° \pm 2.5°$. The magnetic shear (panels a to e), the current density (panels f to j), and the reconnection rate (panels k to o) for IMF clock angle 0° (panels a, f, and k), 45° (panels b, g, and l), 90° (panels c, h, and m), 135° (panels d, i, and n), and 180° (panels e, j, and o). The black lines maximize the quantities represented in each panel. The white arrows correspond to IMF orientation in the (YZ) plane. The terminator is represented by the dashed circle.

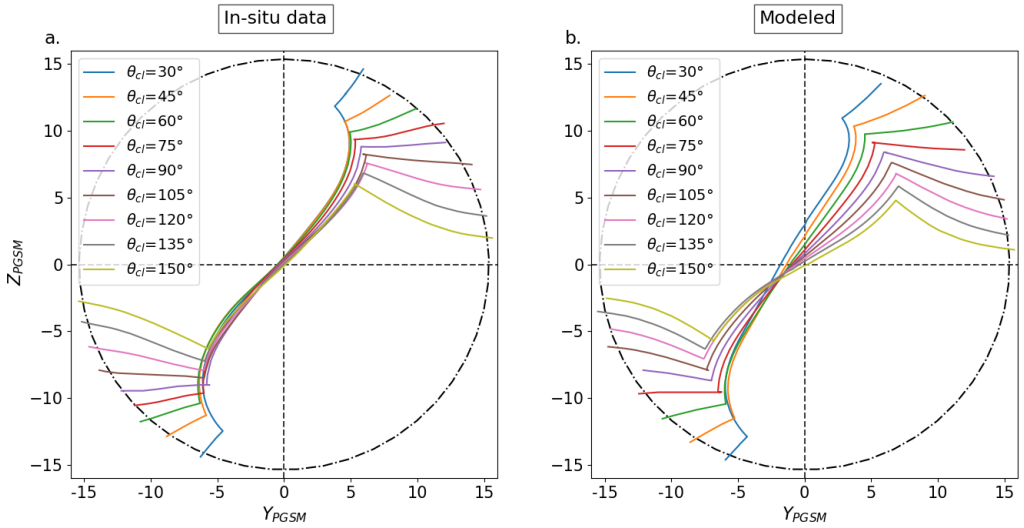

Figure 12. Maximum magnetic Shear Line (MSL) as a function of the IMF clock angle made from global distribution of the magnetic shear made obtained with in-situ measurements ($70° \leq |\theta_{co}| \leq 80°$ and $|\psi| = 0°\pm2.5°$) and analytical models of magnetic fields (T96 ans KF94) in panels a and b, respectively.

and MHD simulations, but not in the KF94 model that assumes draping in vacuum and thus does not account for magnetic reconnection. Finally, for an IMF clock angle of 180° (Fig. 11e) most of the dayside magnetopause exhibits a high magnetic shear and parallel shear angle in both lobes.

For an IMF clock angle of 0° (Fig. 11f), the current density is maximum and exhibits similar amplitudes in both lobes. As the IMF clock angle increases (Fig. 11g,h,i), the amplitude decreases in the lobes and increases in the subsolar region as the magnetic shear angle increases in this region. The magnitude is maximum in the subsolar region for an IMF clock angle of 180° (Fig. 11j) as the magnetic pileup (Fig. 10b) coincides with the anti-parallel region (Fig. 11e). In contrast to the MSLs, the MCLs show a clear dependence on the IMF clock angle. The lines become more inclined toward the equator as the IMF clock angle increases, until they align with the equator for an IMF clock angle of 180° (Fig. 11j).

The reconnection rate exhibits a pattern similar to that of the current density, with high values in the lobes for northward IMF (Fig. 11k), shifting towards the subsolar region as the IMF turns southward (Fig. 11l,m,n), and peaking in the subsolar region for an IMF clock angle of 180° (Fig. 11o). Like the MCLs, but unlike the MSLs, the MRLs become more inclined towards the equator as the IMF clock angle increases.

4.1.2 Intermediate IMF cone angle

Figure 13 shows the magnetic shear (panels a to e), current density (panels f to j), and the reconnection rate (panels k to o) at intermediate IMF cone angle ($20° \leq |\theta_{co}| \leq 30°$) and for a dipole tilt of 0° ($|\psi| = 0°\pm2.5°$) as a function of the IMF clock angle (0°, 45°, 90°, 135°, and 180°).

For an IMF clock angle of 0° (Fig. 13.a), the pattern of the magnetic shear is similar to that seen for a large IMF cone angle (Fig. 11a), but with a thinner (resp. larger) high shear region in the northern (resp. southern) lobe due to the asymmetry of the mag-

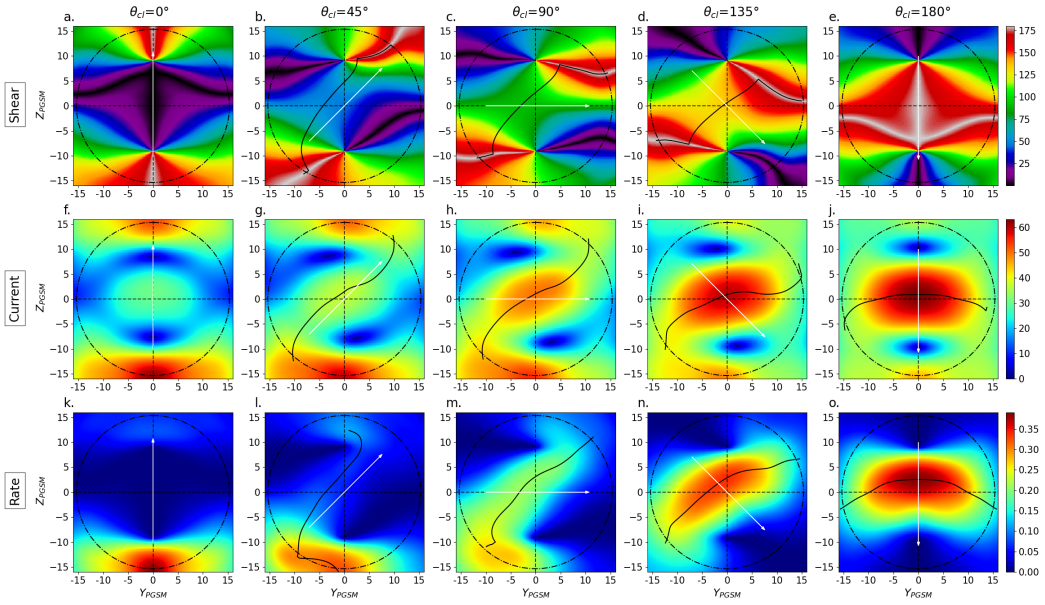

Figure 13. Global distributions of magnetic shear, current density, and reconnection rate at the surface of the magnetopause at intermediate IMF cone angles. Subsets of the measurement for IMF cone angles in the range $20° \leq |\theta_{co}| \leq 30°$ and dipole tilt angles of $|\psi| = 0° \pm 2.5°$. The legend is the same as Figure 11.

netosheath draping between the quasi-parallel and the quasi-perpendicular sides of the magnetopause. However, unlike the case of a large IMF cone angle, the MSLs exhibit a dependence on the IMF clock angle as the IMF turns towards the south (Fig. 13b-d). This is because asymmetry in the magnetic field draping between the quasi-parallel and quasi-perpendicular side of the magnetopause (see Fig. 6.a) affects the spatial variation of the magnetic shear gradient, which is therefore more dependent on the value of the IMF clock angle. Finally, for an IMF clock angle of 180° (Fig. 13.e), the dayside mostly exhibits high magnetic shear but the geometry of the anti-parallel region (along the noon meridian and in the southern hemisphere) prevents the definition of a MSL.

The current density for an IMF clock angle of 0° (Fig. 13f) exhibits a small asymmetry between the north and south lobes, with the latter showing higher values, due to the asymmetry in magnetic strength between the quasi-parallel and quasi-perpendicular sides of the magnetopause (Fig. 10c). The amplitude of the current density in the subsolar region is higher than for large IMF cone angles because of the larger difference in magnitude between the magnetosheath and the magnetospheric magnetic fields, which tends to increase the current density at low magnetic shear. As the IMF turns southward (Fig. 13g-i), the current density decreases in the lobes and increases in the subsolar region, eventually reaching its maximum value in this region for an IMF clock angle of 180° (Fig. 13j). At intermediate IMF cone angles, the MCLs seem to overlap for north to pure east IMF (Fig. 13g,h), and incline towards the equator for southward IMF (Fig. 13i,j). The MCL for an IMF clock angle of 180° extends into the southern hemisphere on the flanks because of the magnetosheath draping asymmetry.

At intermediate IMF cone angles, the global reconnection rate amplitude is about half that of the large IMF cone angle, due to the decrease in magnetic field strength in the magnetosheath between these two regimes (Fig. 10 b and c). The reconnection rate for an IMF clock angle of 0° (Fig. 13k) shows a strong asymmetry between the north and

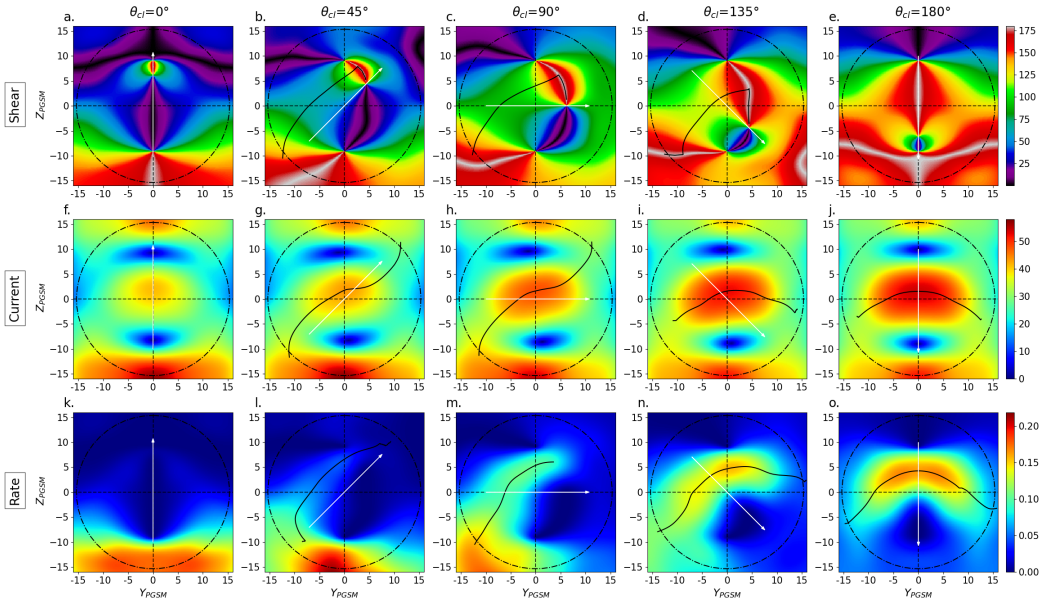

Figure 14. Global distributions of magnetic shear, current density, and reconnection rate at the surface of the magnetopause at small IMF cone angles. Subsets of the measurement for IMF cone angles in the range $|\theta_{co}| \leq 12.5°$ and dipole tilt angles of $|\psi| = 0° \pm 2.5°$. The legend is the same as Figure 11.

south lobes, despite both having a high magnetic shear, due to the difference in amplitude between the quasi-parallel/quasi-perpendicular sides of the magnetic pileup (Fig. 10c). This is interesting because when magnetic shear is considered as the only parameter determining the location of magnetic reconnection, both lobes are equally important, while when reconnection rate is considered, only the south lobe is significant. When the IMF turns southward (Fig. 13l-n), the reconnection rate remains larger on the quasi-perpendicular part of the magnetopause, resulting, for an IMF clock angle of 180° (Fig. 13o), in higher values in the northern hemisphere. The MRLs tend to become more curved and inclined towards the equator as the IMF turns toward south.

4.1.3 Low IMF cone angle

Figure 14 shows the magnetic shear (panels a to e), the current density (panels f to j), and the reconnection rate (panels k to o) at low IMF cone angle ($|\theta_{co}| \leq 12.5°$) and for a dipole tilt of 0° ($|\psi| = 0° \pm 2.5°$) as a function of the IMF clock angle (0°, 45°, 90°, 135°, and 180°).

As described in section 3.3, when the IMF cone angle is low, the areas of anti-parallel and parallel magnetic shear join together at the dayside magnetopause. For an IMF clock angle of 0° (Fig. 14a), most of the dayside magnetopause exhibits low shear values that increase as the IMF turns towards southward (Fig. 14b,c,d,e). Due to the positive sign of the B_x component of the IMF, the southern (resp. northern) lobe remains at high (resp. low) shear for all IMF clock angles. The location of the MSLs changes slightly as the IMF clock angle increases.

At low IMF cone angles, the global current density pattern (Fig. 14f-j) is only weakly affected by the IMF clock angle, since the main contribution to its amplitude comes from the difference in strength between the magnetospheric and magnetosheath magnetic fields.

Another consequence of this difference in strength is that for an IMF clock angle of 0°, the subsolar region (Fig. 14f) has the highest current density values of all IMF cone regimes (Fig. 11f, 13f). As the IMF turns southward, there is a slight increase in the current density in the subsolar region due to an increase in magnetic shear, and a slight decrease in both lobes due to the magnetic pileup in the quasi-perpendicular magnetosheath shifting towards the north lobe at low shear. The change in the shape of the MCLs seems to be due only to the difference in the integration technique, gradient (Fig. 14g and h) and eigenvector of the Hessian matrix (Fig. 14i and j), used to obtain these lines (see section 2.8). It should also be noted that the MCL for an IMF clock angle of 45° (Fig. 14g) passes through a region of parallel magnetic fields (Fig. 14b) where reconnection is impossible, and this would be the same for all IMF clock angles below about 60°.

At low IMF cone angles, the reconnection rate is approximately half that of the intermediate IMF cone angle consistently, again, with the decrease of the magnetic field strength in the magnetosheath between these two regimes (Fig. 10 c and d). In contrast with the current density, the pattern of the reconnection rate is significantly impacted by the IMF clock angle, presenting a strong asymmetry between the quasi-parallel and quasi-perpendicular side of the magnetopause. When the IMF is northward (Fig. 14k,l), the reconnection rate is highest in the southern lobe, where both the magnetic amplitude (Fig. 10d) and magnetic shear (Fig. 14a) are also at their highest. Since the magnetic shear in the northern lobe remains low for all IMF clock angles, the reconnection rate in this region remains extremely small. When the IMF turns southward (Fig. 14l,m,n), the reconnection rate increases on the dayside due to an increase in magnetic shear, and it decreases in the southern lobe as the magnetic pileup in the magnetosheath shifts towards the north lobe. For a pure south IMF (Fig. 14o), the reconnection rate shows the highest values in the northern hemisphere due to the strong asymmetry in the magnetic pileup. However as the high shear areas do not coincide with the magnetic pileup, these reconnection rate values remain smaller than those obtained for northward IMF in the southern lobe. This is interesting because it suggests that for small IMF cone angles, magnetic reconnection is more efficient for northward than for the southward IMF. In contrast to the MCLs, the MRLs appear to show a dependence on the IMF clock angle (Fig. 14k-o). They tend to tilt toward the equator as the IMF turns southward, resulting in a curved line that is mainly in the northern hemisphere for an IMF clock angle of 180°.

4.2 Dependence on the dipole tilt angle

The previous subsection discussed the influence of the IMF clock and cone angles on the global distribution of magnetic shear, current density, and reconnection rate. We now examine how the dipole tilt angle affects the lines that maximize these quantities.

4.2.1 Northward IMF

Figure 15 shows the MSLs (panels a, b, c), MCLs (panels d, e, f), and the MRLs (panels g, h, i) at large (panels a, d, g), intermediate (panels b, e, h) and low (panels c, f, i) IMF cone angle and for an IMF clock angle of 60° as a function of the dipole tilt angle (-20°, -10°, 0°, 10°, and 20°). The global distributions of the quantities used to obtain each of these lines can be found in the supplementary material.

The MSLs exhibit a strong dependence on the dipole tilt angle at large IMF cone angles (Fig. 15a), shifting from a predominantly northern hemisphere location to a southern hemisphere location as the tilt angle increases. In line with expectations, the MSL with a dipole tilt angle of 0° passes through the subsolar point. The same dependence on the dipole tilt angle is observed at intermediate IMF cone angles (Fig. 15b). However, due to the asymmetry in the draping between the quasi-parallel/quasi-perpendicular sides of the magnetopause, the MSLs are shifted towards the northern hemisphere in comparison with the large IMF cone angle case, with the MSL at ψ=20° passing near the

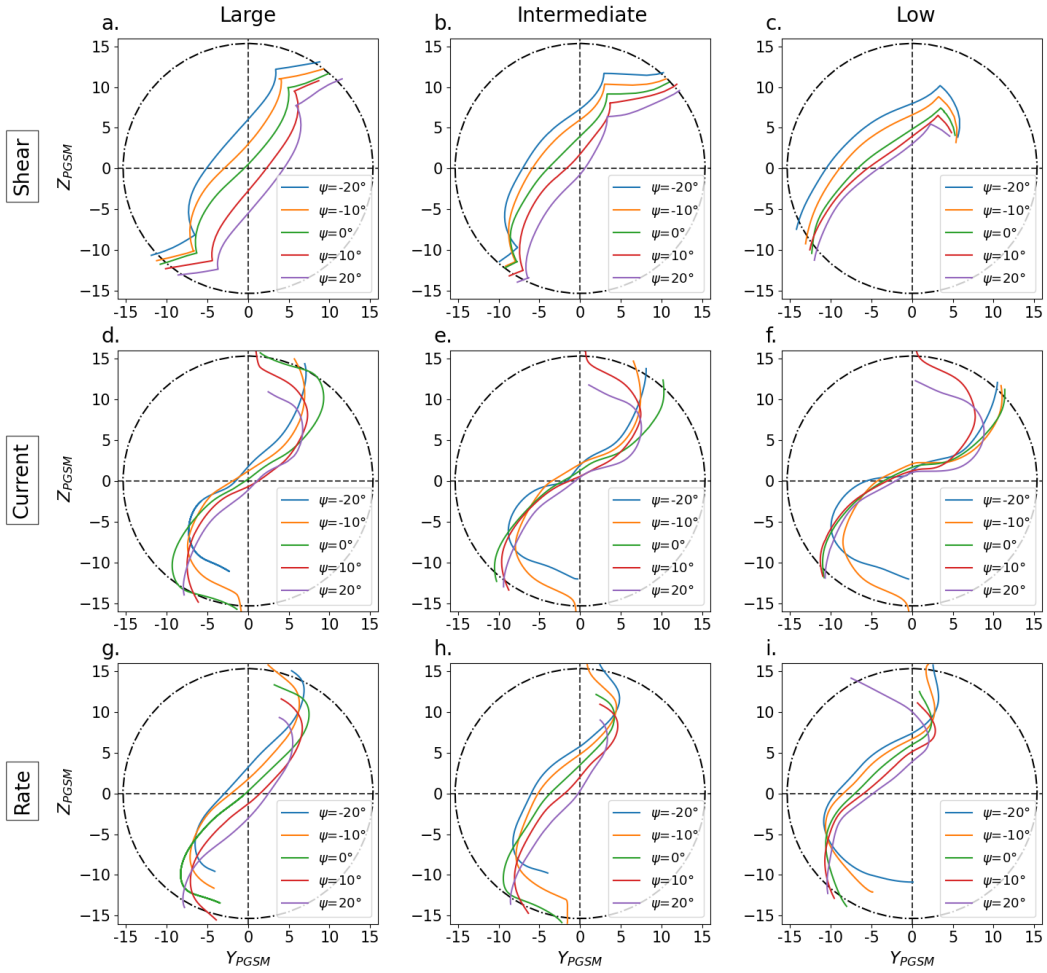

Figure 15. Lines maximizing the magnetic shear (panels a, b, c), the current density (panels d, e, f), and reconnection rate (panels g, h, i) at large (panels a, d, g), intermediate (panels b, e, h) and low (panels c, f, i) IMF cone angle and for an IMF clock angle of 60° as a function of the dipole tilt angle (-20°, -10°, 0°, 10°, and 20°). The dashed circle represents the terminator.

subsolar point. This shift is even more pronounced at low IMF cone angles (Fig. 15c), where all MSLs cross the noon meridian far northward of the subsolar point.

The MCLs show a small dependence on dipole tilt angle at large IMF cone angles (Fig. 16d), crossing the noon meridian in the northern and southern hemispheres for negative and positive dipole tilt angles, respectively. The dependence on the dipole tilt angle appears to decrease as the IMF cone angle decreases in the intermediate and low regimes (Fig. 16e and f). This is because the difference in magnetic field strength between the magnetosphere and the magnetosheath becomes the main contributor to the current density amplitude. The influence on the dipole tilt angle seems to be visible only at higher latitudes in the northern and southern hemispheres for positive and negative dipole tilt values, respectively.

Similarly to the MSLs, the MRLs show a dependence to dipole tilt angle across all the IMF cone angles regimes (Fig. 16g, h, and i) as expected given the strong dependence of the reconnection rate on the magnetic shear.

4.2.2 Southward IMF

Figure 16 shows the MSLs (panels a, b, c), MCLs (panels d, e, f), and MRLs (panels g, h, i) at large (panels a, d, g), intermediate (panels b, e, h) and low (panels c, f, i) IMF cone angle and for an IMF clock angle of 120° as a function of the dipole tilt angle (-20°, -10°, 0°, 10°, and 20°).

The MSLs (Fig. 16.a, b, and c) show the same strong dependence on the dipole tilt angle as in the northward case.

In contrast with the northward IMF case, the MCLs do not seem to exhibit a clear dependence on the dipole tilt angle at large IMF cone (Fig. 16d). In fact, the maximum values of the current change position slightly as the dipole tilt angle varies (see Supplementary Material). However, these maxima are shifted along the average orientation of the MCLs. This keeps the lines relatively close to each other. Similar to the northward IMF case, the significant amplitude difference in magnetic field strength diminishes the influence of the dipole tilt angle as the IMF cone angle decreases in the intermediate and low regimes (Fig. 16e and f).

Similar to the current density, the shift of the global pattern (see Supplementary Materials) along the average orientation of the MRLs (Fig. 16g) leaves them unaffected by the dipole tilt angle variation for large IMF cone angles. As the IMF cone decreases into the intermediate and low regimes (Fig. 16h and g), the influence of the dipole tilt angle becomes apparent due to the asymmetry in magnetic field amplitude between the quasi-parallel and quasi-perpendicular sides of the magnetosheath.

Figure 17 shows the MCLs (panels a, b, c), and the MRLs (panels d, e, f) at large (panels a, d,), intermediate (panels b, e) and low (panels c, f) IMF cone angle and for an IMF clock angle of 180° as a function of the dipole tilt angle (-20°, -10°, 0°, 10°, and 20°). The global distributions of the quantities used to obtain each of these lines can be found in the supplementary material. Figure 17 does not show MSLs because, as mentioned in the method section 2.8, we do not determine them for an IMF clock angle of 180°. However, the spatial distribution of the magnetic shear can be found in supplementary materials.

The MCLs for large IMF cone angle (Fig. 17a) show a dependence on the dipole tilt angle in the flanks but converge toward the equator in the subsolar region. The behavior of the MCLs in the subsolar region is influenced by three factors. First, for an IMF clock angle of 180°, the noon meridian displays anti-parallel magnetic shear between the cusps (Fig. 11e). Second, the values of the magnetospheric magnetic field strength at the subsolar point remain maximum (47.4 nT ± 1.6 nT) regardless of the dipole tilt an-

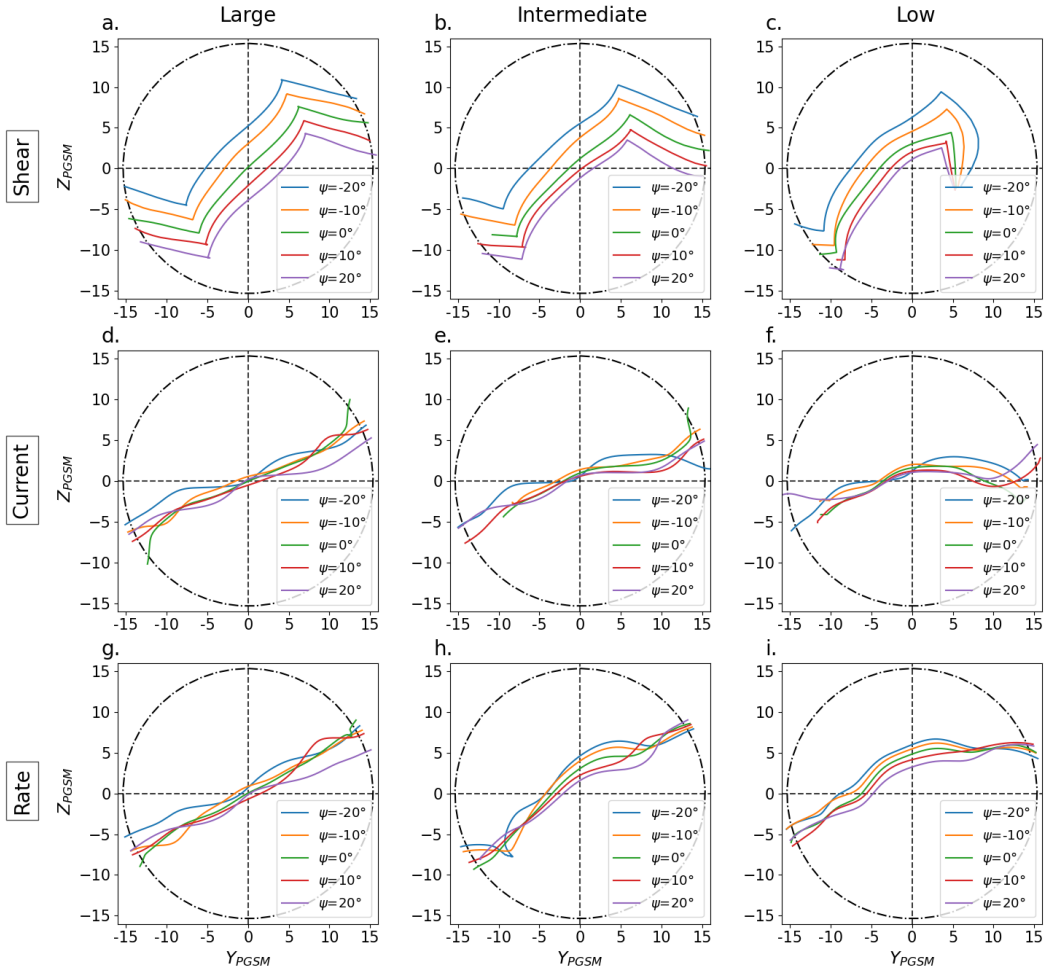

Figure 16. Lines maximizing the magnetic shear (panels a, b, c), the current density (panels d, e, f), and reconnection rate (panels g, h, i) at large (panels a, d, g), intermediate (panels b, e, h) and low (panels c, f, i) IMF cone angles and for an IMF clock angle of 120° as a function of the dipole tilt angle (-20°, -10°, 0°, 10°, and 20°). The dashed circle represents the terminator.

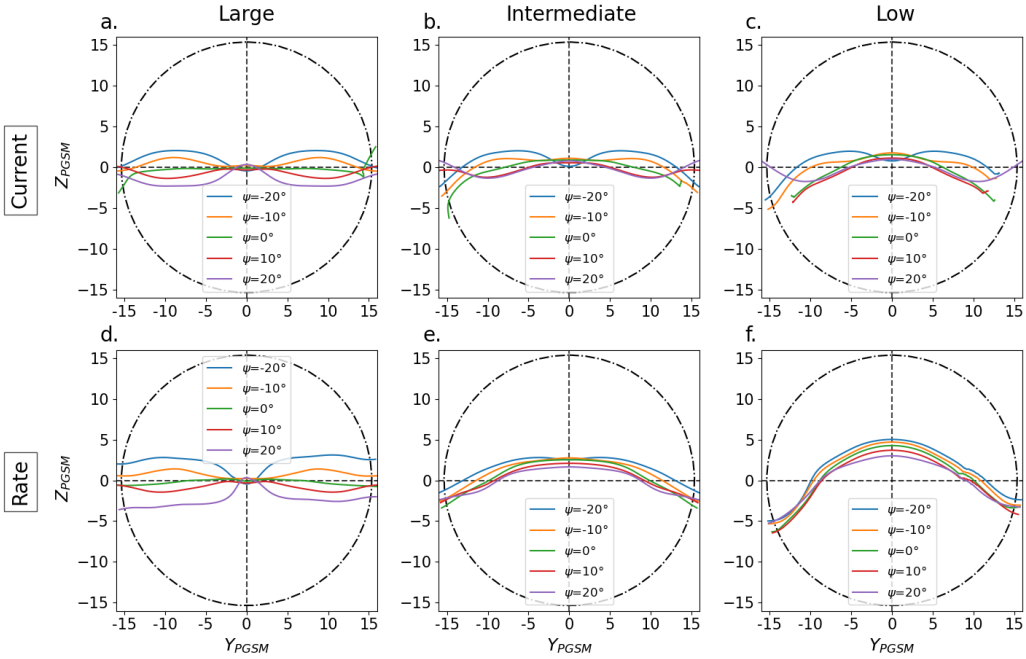

Figure 17. Lines maximizing the current density (panels a, b, c), the reconnection rate (panels d, e, f), at large (panels a, d), intermediate (panels b, e) and low (panels c, f) IMF cone angles and for an IMF clock angle of 180° as a function of the dipole tilt angle (-20°, -10°, 0°, 10°, and 20°). The dashed circle represents the terminator.

gles. Lastly, the magnetic pileup in the magnetosheath peaks near the subsolar point (Fig. 10b). Therefore the current is also maximum near the subsolar point and the effect of the dipole tilt angle is only visible on the flanks. As the IMF cone angle decreases into the intermediate and low regimes (Fig. 17b and c), the dependence of the MCLs on the dipole tilt angle becomes less clear for $\psi \geq 0°$.

The MRLs for large IMF cone angles (Fig. 17d) show a strong dependence on the dipole tilt angle in the flanks but come back toward the equator in the subsolar region for the reasons detailed above for the MCLs (Fig. 17a). Interestingly, their shape seem quite consistent with separators obtained with global MHD simulations in a study of the effect of dipole tilt on magnetic reconnection (Eggington et al. 2020 (Eggington et al., 2020)). The location of the MRLs show only a small dependence on the dipole tilt angle in the intermediate and low IMF cone angle regimes (Fig. 17e and f). Their shape, which favors the northern hemisphere (i.e. aligned with the quasi-perpendicular bow shock) for all tilt angle values, seems surprising. Even more so since the draping asymmetry between the quasi-parallel/quasi-perpendicular side of the magnetopause tends to produce the highest magnetic shears in the southern hemisphere (Fig. 13e and Fig. 14e). However, their shape and location result from the large amplitude of the magnetosheath magnetic field in the northern hemisphere (here quasi-perpendicular side of the magnetosheath). The overall evolution of the location, shape, and ordering of the MRLs (subsolar region in panel d; panels e and f) shows that the reconnection rate, once the magnetic shear is sufficiently high, is primarily controlled by the amplitude of the magnetosheath magnetic field, and secondarily by the magnetospheric magnetic strength. However, when the variation amplitude of the magnetosheath magnetic field is relatively isotropic (Fig. 10b), a small difference in magnetic shear and amplitude of the magnetospheric mag-

netic field seems to have a strong effect on the location of the MRLs (away of subsolar region in Fig. 17d).

5 Global and local approaches on magnetic reconnection

Section 4 explored the influence of the IMF orientation and dipole tilt angle on the global distribution of the magnetic shear angle, current density, and reconnection rate and on the lines maximizing these quantities. Such maximization can be considered a global approach, as it requires knowledge of the global spatial variation of a quantity to identify a possible X-line. Thus, the underlying idea would be that the localization of the magnetic reconnection is controlled by global constraints at the magnetopause. In parallel, several numerical modeling studies (Schreier et al., 2010; Hesse et al., 2013; Y.-H. Liu et al., 2015; Aunai et al., 2016; Y.-H. Liu et al., 2018) focused on determining the orientation of reconnection lines with an initially homogeneous current sheet, which can therefore be characterized as a local approach to determining how X-line develop. For most of the local studies (Hesse et al., 2013; Y.-H. Liu et al., 2015; Aunai et al., 2016; Y.-H. Liu et al., 2018), the X-line is found to bisect the magnetic fields on each side of the magnetopause. Although it can be expected that global and local approaches will results in different X-line orientations, the extent of these difference is unknown. This is the aim of this section, in which we compare the line maximizing magnetic shear used in the Maximum Magnetic Shear model (Trattner et al., 2007) with the line following the bisection from the subsolar point. Here, the local bisection orientation is chosen, in contrast to, say, the direction that maximizes Cassak-Shay formula because it seems to better agree with previously published simulations(Hesse et al., 2013; Y.-H. Liu et al., 2015; Aunai et al., 2016; Y.-H. Liu et al., 2018). Tests (not shown here) have shown that following the local orientation maximizing the Cassak-Shay formula was anyway following a very similar path.

Fig. 18a shows the color coded spatial distribution of the magnetic shear angle for a IMF cone angle of $80° \leq |\theta_{co}| \leq 90°$, an IMF clock angle of 130°, and a dipole tilt angle of $\psi = 0° \pm 2.5°$ for the magnetosphere. Along the MSL is represented the local and bisecting orientations (small black lines) of the magnetic field vector on each side of the magnetopause (green and blue arrows for the magnetic field of the magnetosphere and magnetosheath, respectively). As expected, the magnetic field vectors are in agreement with the shear angle map, exhibiting anti-parallel behavior in white regions and forming an angle of approximately 130° in the subsolar region. It is important to notice that the bisection orientations are not aligned with the local tangents of the MSL which demonstrates that the global and local approaches are not consistent with each other. The angular differences are large in the anti-parallel region, where the local bisections are nearly perpendicular to the MSL, and smaller in the subsolar region. However, a global X-line obtained by following the local bisections from this region gives a prediction significantly different from the MSL. More than the distance between the lines, the fundamental difference between these two candidate X-lines is that the bisection line cannot align with the anti-parallel regions for any IMF orientation, except for IMF clock angle of 180°. However, observations of accelerated cusp ions (Trattner et al., 2007, 2021) and MHD simulations for northward IMF (Komar et al., 2015) show that magnetic reconnection occurs along the anti-parallel regions. From the same reasoning, it is thus worth noting, at this point, that the line maximizing the reconnection rate distribution visible on figures 11, 13 and 14 have also no reason to locally align with the orientation maximizing the Cassak-Shay formula even though this local orientation is necessary to produce the map in the first place. Understanding to what extent lines constructed from a local approach would differ from the MRLs is, however, not trivial as the result critically depends on the choice of an "initial" point to integrate from, in contrast to the global approach. While the choice of the subsolar point in Fig. 18**a** seems reasonable, it may not be true

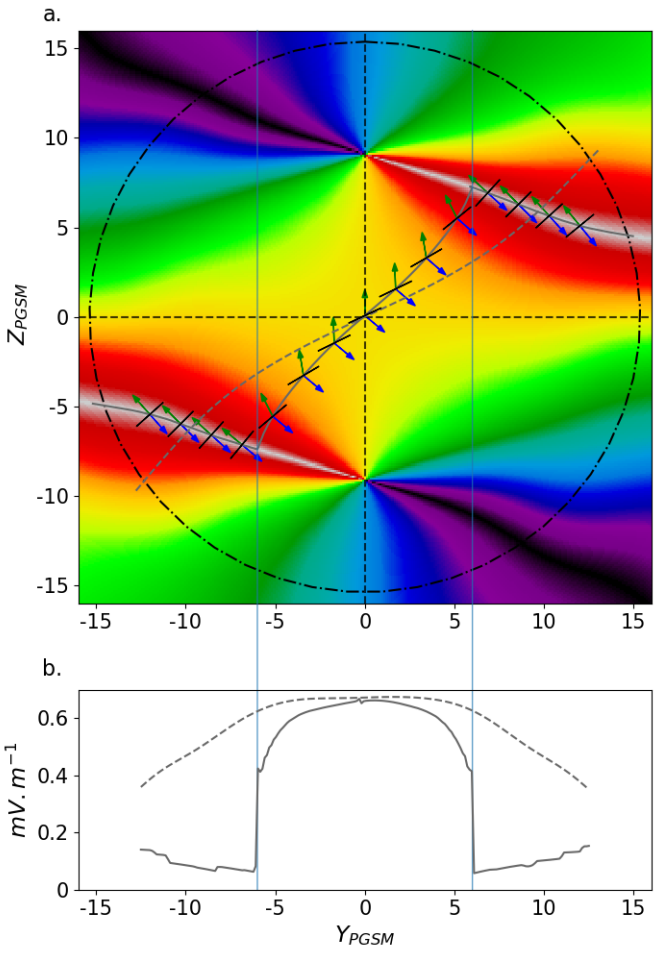

Figure 18. Global distribution of the magnetic shear represented in panel a, using in-situ measurements for a IMF cone angle of $80° \leq |\theta_{co}| \leq 90°$, an IMF clock angle has a value of 130°, and a dipole tilt angle of $\psi = 0° \pm 2.5°$ for the magnetosphere. The solid gray line is the MSL, along which the orientation of the magnetospheric and magnetosheath magnetic fields are indicated by the green and blue arrows, respectively. The small black lines correspond to the local bisections of the magnetic fields. The dashed gray line follow the local bisection of the magnetic fields, as integrated from the subsolar point. In panel b, the reconnection rate along the MSL and the bisection line are shown as solid and dashed lines, respectively. The vertical blue lines mark where the component reconnection part of the MSL joins the anti-parallel branches.

generally when any IMF orientation and dipole tilt are considered, and will be the topic of a forthcoming study.

Fig. 18b shows the reconnection rate along the MSL and the bisection line if magnetic merging were to occurs there. In contrast to the reconnection rate discussed in the previous section, for which the merging components are determined by maximizing its values (section 2.6.3), here these components are those which are perpendicular to the local tangents of the two candidate X-lines. If the reconnection rate for these lines is similar at the subsolar point, the one associated with the MSL decreases to approximately 0.4 mV/m before the component reconnection part of the MSL joins the anti-parallel branches (vertical blue lines). A discontinuity is present at the junction to the anti-parallel branches, where the reconnection rate suddenly drops to 0.06 mV/m before slowly increasing to approximately 0.15 mV/m in the flanks. This drastic reduction of the reconnection rate in the anti-parallel magnetic shear region results from the orientation of the MSL is associated with really small reconnecting component. In contrast, the reconnection rate along the bisection line remains almost constant with a value of about 0.61 mV/m until the line reaches the anti-parallel regions, and then decreases to 0.34 mV/m. The decrease in the reconnection rate occurs where the magnetic shear along the bisection line is the highest. An increase in the magnetic shear should increase the amplitude of the reconnected components (Eq. 6). However, the reconnection rate decreases due to the reduction in the amplitude of the magnetic field in the magnetosphere and magnetosheath (Fig. 10a and b).

6 Discussion and Conclusion

Both numerical simulations and observations support the existence of extended reconnection lines on the magnetopause surface. Their location, as a function of the IMF orientation and dipole tilt angle, constitutes a long standing question in magnetospheric physics. Historically, the spatial distribution of the shear angle between the draped magnetosheath magnetic field and the magnetospheric field, has been the primary parameter used to build models predicting the location of such global X-lines. Besides the obvious importance of the magnetic shear in the reconnection process, other quantities such as the current density and the reconnection rate, could be thought as equally determinant for localizing the reconnection line. Especially, since these quantities strongly depend on the magnetic shear, but also on the plasma density and/or the amplitude of magnetic fields. However, until now, the spatial distribution of these quantities on the magnetopause and their dependence on the IMF orientation and dipole tilt is still poorly understood. Furthermore, these spatial distributions, including that of the magnetic shear angle, have so far only been obtained from analytical or numerical models, and never entirely constrained by observational means.

In this study, we proposed the first global reconstruction of the spatial distribution of magnetic shear, current density, and an MHD reconnection rate scaling law on the dayside magnetopause from in-situ spacecraft measurements only. These distributions and their dependence on the IMF orientation and dipole tilt angle have been analyzed. A line maximizing the considered quantity has been computed and discussed as a possible X-line candidate.

6.1 Spatial distributions of the magnetic shear, current density, and reconnection rate

The first outcome of this study concerns the distribution of the magnetic shear angle. A comparison between the magnetic shear maps obtained with in-situ measurements and those obtained with models showed that there is a relatively good agreement between the two for large ($|\theta_{co}| \geq 45^{\circ} \pm 5^{\circ}$) and small ($|\theta_{co}| \leq 12.5^{\circ} \pm 2.5^{\circ}$) IMF cone angles. However, significant differences were found at intermediate IMF cone angles ($12.5^{\circ} \pm 2.5^{\circ} \leq$

$|\theta_{co}| \leq 45^{\circ} \pm 5^{\circ}$) because the KF94 model predicts invalid magnetosheath field draping for such IMF orientations (Michotte de Welle et al., 2022). Despite their qualitative agreement, the maximum shear maps obtained from models and observations lead to maximum shear lines that differ in their response to varying IMF clock angles. In contrast to those obtained from models, maximum shear lines at large IMF cone angles obtained from observations are found to be relatively independent of the IMF clock angle in the component reconnection region. This behavior appears consistent with results from global MHD simulations performed in similar IMF conditions (Komar et al., 2015). The dependence of maximum shear lines with the dipole tilt angle is important and similar to that already reported in previous studies (Trattner et al., 2021), with a shift to northern (resp. southern) latitudes for negative (resp. positive) tilt angles.

A drawback of considering only the magnetic shear is that it disregards the impact of the magnetic field amplitude on reconnection, although it is well known to be important in reconnection physics. The distribution of the magnetic amplitude on the magnetopause and its jump across the layer is, however, considered in the current density and the reconnection rate scaling laws. The reconstructed distributions of the current density and the reconnection rate were found to be consistent with those obtained from published MHD simulations results (Komar et al., 2015; Souza et al., 2017; Glocer et al., 2016). The current density amplitude is also found to be consistent with that observed in-situ (Haaland et al., 2020; Lukin et al., 2020; Beedle et al., 2022). Although the current density and reconnection rate scaling law both factor in the magnetic shear, their distributions are found to be very different from that of the magnetic shear. They are, however, relatively similar to each other. This similarity between the current and reconnection rate distributions, and their respective maximum line, is more pronounced for large IMF cone angles, and fades away as the IMF becomes increasingly radial due to their different dependence on the amplitude of the magnetic field. Indeed the current density becomes primarily results from the difference in the amplitude of the upstream magnetic fields for increasingly radial IMF conditions, whereas the reconnection rate depends on the magnetic shear and the absolute amplitude of reconnecting magnetic components rather than their difference. One of the important consequences for the current density is that its distribution becomes weakly dependent on the IMF clock angle and dipole tilt angle as the IMF becomes more radial, in contrast to the distribution of the reconnection rate. Contrary to the lines obtained from maximizing the magnetic shear, those obtained from the current density or the reconnection rate do not present sharp turns, which is a specificity of the maximum shear model.

The spatial distributions of the current density and reconnection rate were found to be more complex than that of the shear angle. In particular, in the case of the current density, we observed the possible appearance of several local maxima originating from the fact that the current can be large either because of a large jump in the magnetic amplitude or in the magnetic orientation, whose behaviors are relatively independent. This results in a necessary choice among different maximization lines for which a physical constraint would remain to be found. We also found that certain configurations unfavorable to the merging process, such as those with low magnetic shear and strong asymmetry between magnetospheric and magnetosheath magnetic field strengths, can still result in significant current density. Furthermore, some IMF orientations results in lines maximizing the current density passing through regions of parallel magnetic fields, where reconnection is *de facto* impossible. Therefore, even though the current density is an important feature of the magnetopause and could also be important for aspects of reconnection such as its onset and/or propagation, it seems unlikely that a global X-line can be determined by the sole maximization of the current density distribution.

6.2 Discriminating between the X-line candidates

The three quantities analyzed in this study display distinct characteristics and dependence on the IMF orientation and dipole tilt angles. Therefore observations of magnetic reconnection in certain ranges of these parameters should allow to discriminate between the different X-line models (if any applies). For instance, observations made for intermediate and low IMF cone angles should allow us to distinguish between the lines maximizing the current density and those maximizing the magnetic shear or the reconnection rate. Indeed, the dependence of current density on IMF clock and dipole tilt angle decreases when the IMF cone angle decreases, which is not true for the other two quantities. In contrast, the lines maximizing the magnetic shear and the reconnection rate are relatively similar, except for strongly southward IMF, at intermediate and low IMF cone angle. This would make them difficult to distinguish from each other, especially considering the uncertainty in the determination of the causal IMF. However, for large IMF cone angles, the maximum reconnection rate lines incline towards the equator as the IMF clock angle increases, which fact does not occur for the component reconnection part of the maximum magnetic shear lines. Thus, observations of magnetic reconnection at high latitudes or in the magnetopause flanks should allow to discriminate between these two X–line candidates. Furthermore, at large IMF cone angles, some IMF clock angles produce reconnection rate distributions resulting in lines that are mostly independent of the dipole tilt angle, while the lines maximizing the magnetic shear remains strongly dependent on it. Finally, a unique feature distinguishes the lines maximizing magnetic shear from those maximizing other quantities is that it follows the region of anti-parallel shear, provided that the IMF clock angle is not strongly southward.

6.3 Global and local approaches of an X-line

No matter which quantity is considered, X-lines were obtained by maximizing a quantity defined on a global scale. The physics underlying the formation of such extended X-lines remains, however, unclear. In one scenario, these regions could be those of preferred reconnection onset, resulting from the global scale interaction of the solar wind and IMF with the magnetosphere. In another, extended X-lines could result from a localized onset followed by X-line spreading governed by local plasma mechanisms. Other scenarios mixing global and local constraints may also be imagined, for instance where X-lines develop and orient along a direction imposed by local physics but only one exist due to some large scale constraint. It is also possible that X-lines orient in such a way imposed by local physics but inconsistently with global scale constraints, resulting in the formation of flux ropes as proposed by Liu et al., JGR (2018) (Y.-H. Liu et al., 2018) and Genestreti et al. 2022 (Genestreti et al., 2022).

In this study, we have shown the X-line built from maximizing a given quantity distributed on the magnetopause is locally oriented along directions disagreeing with predictions suggested by local physics, and therefore these two scenarios are not consistent with each other.

Local studies (Hesse et al., 2013; Y.-H. Liu et al., 2015; Aunai et al., 2016; Y.-H. Liu et al., 2018) tend to agree that magnetic reconnection appears to be oriented along the bisection of the upstream magnetic fields. However, the construction of a global X-line following this local approach critically depend on the onset location of magnetic reconnection, and therefore requires further constraints to be defined. For instance, the onset location could be situated at point of first contact of the IMF with the magnetopause as used in this study, it can also be where the reconnecting component are the greatest (Moore et al., 2002), or it might be located elsewhere. More importantly, since following the bisection does not take into account the spatial variation of physical quantities such as magnetic shear or magnetic field amplitude, it can produce X-lines located where reconnection is unlikely or even impossible, such as in regions of parallel magnetic fields.

An X-line following the global approach, such as the maximum magnetic shear model (Trattner et al., 2007), can result in local merging orientation producing small reconnecting component of the magnetic fields, and therefore, small reconnection rate. Indeed, except for strongly southward IMF, the parts of the MSL along the anti-parallel branches are often close to being parallel to the magnetic field orientation on both sides of the magnetopause. More importantly, an abrupt change in orientation of an X-line, such as the junction between the component and anti-parallel parts of the MSL, tends to produce discontinuities in the reconnection rate along the X-line, and is not seen in other X-line scenarios.

6.4 Limitations and perspectives

For reconstructing the spatial distributions of quantities such as the magnetic field, this study assumes that the influence of magnetic reconnection can be neglected on a large scale, therefore subsets of magnetosheath measurements were selected based solely on the IMF cone angle values and maps for specific clock angles were thus produced in the PGSM coordinate system. However, studies tend to show that magnetic reconnection could have a global effect on the ion density and magnetic field (Phan et al., 1994; Anderson et al., 1997; Kaymaz, 1998). Such an effect could marginally change the distributions of quantities such as magnetic shear, current density, and reconnection rate. Investigations (not included in this report) revealed minor alterations, such as the detailed curvature of magnetic field lines in the magnetosheath, that do not affect the findings of this study but call for more detailed and future work.

The distributions of the potential reconnection rate proposed in this study should be considered with care. First, the reconnection rate was estimated from an MHD scaling law designed for asymmetric conditions but antiparallel field lines. Then, global MHD simulations seems to indicate (Komar & Cassak, 2016) that this law generally under-estimates the measured reconnection rate in conditions different than due southward IMF. Furthermore, it has also been shown that the reconnection rate in asymmetric and non-coplanar current sheets may critically depend on ion kinetic effects (Hesse et al., 2013). Several other effects may alter the reconnection rate at the magnetopause, such as the presence of heavy ions (Toledo-Redondo et al., 2021) or the plasma beta and possible diamagnetic drift of the X-line (Swisdak et al., 2003). More work is thus needed to improve the prediction of the potential reconnection rate on the magnetopause surface and produce more realistic maps.

This study has brought new constraints to where reconnection could be located on the magnetopause, from an observational standpoint. Although also generally the case in other studies, we feel an important limitation of our results comes from assuming steady upstream conditions. Work is being done to reconstruct the time dependent distribution of a given quantity on the magnetopause in varying upstream conditions accounting for the propagation in the magnetosheath, and will be the focus of a forthcoming study.

Although they are among the main parameters conditioning reconnection at the magnetopause, we have here only considered a dependency on the IMF orientation and dipole tilt. The role of other parameters, such as the solar wind Mach number, should be investigated in the future. Also, we assumed the state of the magnetopause only depends on upstream conditions in the solar wind. In reality, the location of X-lines may also depend on the system's more or less recent history, and this should also be investigated.

In addition to addressing the limitations mentioned above, future work should also assess the difference between X-lines produced with the local and global approaches more extensively. The comparison established in Fig. 18 could, for instance, be systematically done for several combinations of IMF orientations and dipole tilt angles. Comparing the line obtained from the global maximization of the reconnection rate distribution and that

obtained from following the local direction maximizing the rate scaling law should also be explored. Future work should also check to what extent X-lines obtained from either the local and global approach locally differ in their orientation from the LMN coordinates often used to analyse spacecraft data (Phan et al., 2014) and orientations predicted from reconstruction methods (Denton et al., 2023). Future studies should also focus on gathering statistical evidences from reconnection signatures to discriminate among all possible scenarios. One idea could be to determine which X-line model best fits the location of the various electron diffusion regions reported in the literature (Lenouvel et al., 2021). Another idea could consist in extracting reconnection signatures massively from decades of data from multiple spacecraft missions, and correlating them with environmental maps such as those used in this study. Work is currently being undertaken in that regard.

Data Availability Statement

The in-situ data are available by using the Speasy package (Jeandet & Schulz, 2023). It allows to access the data on the CDAweb database (`https://cdaweb.gsfc.nasa.gov`) for the THEMIS mission, and AMDA (Budnik, 2011) for Cluster, DoubleStar, and MMS missions.

Acknowledgments

We would like thanks Karlheinz Trattner for his availability and the instructive discussions. We would also like to thank the referees for their constructive comments that allowed us to improve our manuscript. We are grateful to the CDPP/AMDA and the CSA for the data access. We acknowledge use of NASA/GSFC's Space Physics Data Facility's CDAWeb service, and OMNI data Computing resources used for the data analysis have been funded by the Plasapar federation. The corresponding author is funded by the Paris-Saclay University.

References

Alexeev, I. I., Sibeck, D. G., & Bobrovnikov, S. Y. (1998, April). Concerning the location of magnetopause merging as a function of the magnetopause current strength. , *103*(A4), 6675-6684. doi: 10.1029/97JA02863

Anderson, B. J., Phan, T. D., & Fuselier, S. A. (1997, May). Relationships between plasma depletion and subsolar reconnection. , *102*(A5), 9531-9542. doi: 10.1029/97JA00173

Aunai, N., Hesse, M., Lavraud, B., Dargent, J., & Smets, R. (2016, August). Orientation of the X-line in asymmetric magnetic reconnection. *Journal of Plasma Physics*, *82*(4), 535820401. doi: 10.1017/S0022377816000647

Auster, H. U., Glassmeier, K. H., Magnes, W., Aydogar, O., Baumjohann, W., Constantinescu, D., ... Wiedemann, M. (2008, December). The THEMIS Fluxgate Magnetometer. , *141*(1-4), 235-264. doi: 10.1007/s11214-008-9365-9

Axford, W. I. (1969, January). Magnetospheric convection. *Reviews of Geophysics and Space Physics*, *7*, 421-459. doi: 10.1029/RG007i001p00421

Balogh, A., Carr, C., Acuña, M., Dunlop, M., Beek, T., Brown, P., ... Schwingenschuh, K. (2001, 10). The cluster magnetic field investigation: Overview of in-flight performance and initial results. *Annales Geophysicae*, *19*. doi: 10.5194/angeo-19-1207-2001

Baumjohann, W., & et al. (2012). *Basic Space Plasma Physics (Revised Edition)*. doi: 10.1142/9781848168961

Beedle, J. M. H., Gershman, D. J., Uritsky, V. M., Phan, T. D., & Giles, B. L. (2022, February). A Systematic Look at the Temperature Gradient Contribution to the Dayside Magnetopause Current. , *49*(4), e97547. doi:

10.1029/2021GL097547

Borovsky, J. E. (2013, May). Physical improvements to the solar wind reconnection control function for the Earth's magnetosphere. *Journal of Geophysical Research (Space Physics)*, *118*(5), 2113-2121. doi: 10.1002/jgra.50110

Borovsky, J. E., & Birn, J. (2014, February). The solar wind electric field does not control the dayside reconnection rate. *Journal of Geophysical Research (Space Physics)*, *119*(2), 751-760. doi: 10.1002/2013JA019193

Borovsky, J. E., Hesse, M., Birn, J., & Kuznetsova, M. M. (2008, July). What determines the reconnection rate at the dayside magnetosphere? *Journal of Geophysical Research (Space Physics)*, *113*(A7), A07210. doi: 10.1029/2007JA012645

Breuillard, H., Dupuis, R., Retino, A., Le Contel, O., Amaya, J., & Lapenta, G. (2020, September). Automatic classification of plasma regions in near-Earth space with supervised machine learning: application to Magnetospheric Multi Scale 2016-2019 observation. *Frontiers in Astronomy and Space Sciences*, *7*, 55. doi: 10.3389/fspas.2020.00055

Budnik, B. M. R. B. A. N. G. V. . J. C., E. (2011). *AMDA [Database].* Retrieved from `http://amda.irap.omp.eu` doi: 10.6096/2011

Carr, C., Brown, P., Zhang, T. L., Gloag, J., Horbury, T., Lucek, E., ... Richter, I. (2005, Nov). The Double Star magnetic field investigation: instrument design, performance and highlights of the first year's observations. *Annales Geophysicae*, *23*(8), 2713-2732. doi: 10.5194/angeo-23-2713-2005

Cassak, P. A., & Fuselier, S. A. (2016, January). Reconnection at Earth's Dayside Magnetopause. In W. Gonzalez & E. Parker (Eds.), *Magnetic reconnection: Concepts and applications* (Vol. 427, p. 213). doi: 10.1007/978-3-319-26432-5_6

Cassak, P. A., & Otto, A. (2011, July). Scaling of the magnetic reconnection rate with symmetric shear flow. *Physics of Plasmas*, *18*(7), 074501. doi: 10.1063/1.3609771

Cassak, P. A., & Shay, M. A. (2007, October). Scaling of asymmetric magnetic reconnection: General theory and collisional simulations. *Physics of Plasmas*, *14*(10), 102114. doi: 10.1063/1.2795630

Cooling, B. M. A., Owen, C. J., & Schwartz, S. J. (2001, September). Role of the magnetosheath flow in determining the motion of open flux tubes. , *106*(A9), 18763-18776. doi: 10.1029/2000JA000455

Cowley, S. W. H., & Owen, C. J. (1989, November). A simple illustrative model of open flux tube motion over the dayside magnetopause. , *37*(11), 1461-1475. doi: 10.1016/0032-0633(89)90116-5

Crooker, N. U. (1979, March). Dayside merging and cusp geometry. , *84*(A3), 951-959. doi: 10.1029/JA084iA03p00951

Daly, P. W., Saunders, M. A., Rijnbeek, R. P., Sckopke, N., & Russell, C. T. (1984, June). The distribution of reconnection geometry in flux transfer events using energetic ion, plasma and magnetic data. , *89*(A6), 3843-3854. doi: 10.1029/JA089iA06p03843

Daughton, W., & Karimabadi, H. (2005, March). Kinetic theory of collisionless tearing at the magnetopause. *Journal of Geophysical Research (Space Physics)*, *110*(A3), A03217. doi: 10.1029/2004JA010751

Denton, R. E., Liu, Y., Agudelo Rueda, J., Genestreti, K. J., Hasegawa, H., Hosner, M., ... L., B. J. (2023). Determining the orientation of a magnetic reconnection X line and implications for a 2D coordinate system. doi: 10.22541/essoar.169841445.51137545/v1

Dimmock, A. P., Hietala, H., & Zou, Y. (2020, June). Compiling Magnetosheath Statistical Data Sets Under Specific Solar Wind Conditions: Lessons Learnt From the Dayside Kinetic Southward IMF GEM Challenge. *Earth and Space Science*, *7*, 01095. doi: 10.1029/2020EA001095

Dimmock, A. P., & Nykyri, K. (2013, August). The statistical mapping of magnetosheath plasma properties based on THEMIS measurements in the magnetosheath interplanetary medium reference frame. *Journal of Geophysical Research (Space Physics)*, *118*(8), 4963-4976. doi: 10.1002/jgra.50465

Dimmock, A. P., Nykyri, K., & Pulkkinen, T. I. (2014, August). A statistical study of magnetic field fluctuations in the dayside magnetosheath and their dependence on upstream solar wind conditions. *Journal of Geophysical Research (Space Physics)*, *119*(8), 6231-6248. doi: 10.1002/2014JA020009

Dimmock, A. P., Pulkkinen, T. I., Osmane, A., & Nykyri, K. (2016, May). The dawn-dusk asymmetry of ion density in the dayside magnetosheath and its annual variability measured by THEMIS. *Annales Geophysicae*, *34*(5), 511-528. doi: 10.5194/angeo-34-511-2016

Drake, J. F., & Lee, Y. C. (1977, August). Kinetic theory of tearing instabilities. *Physics of Fluids*, *20*(8), 1341-1353. doi: 10.1063/1.862017

Dungey, J. W. (1961, January). Interplanetary Magnetic Field and the Auroral Zones. , *6*(2), 47-48. doi: 10.1103/PhysRevLett.6.47

Dunlop, M. W., Zhang, Q. H., Bogdanova, Y. V., Lockwood, M., Pu, Z., Hasegawa, H., ... Liu, Z. X. (2011, July). Extended Magnetic Reconnection across the Dayside Magnetopause. , *107*(2), 025004. doi: 10.1103/PhysRevLett.107.025004

Eggington, J. W. B., Eastwood, J. P., Mejnertsen, L., Desai, R. T., & Chittenden, J. P. (2020, July). Dipole Tilt Effect on Magnetopause Reconnection and the Steady-State Magnetosphere-Ionosphere System: Global MHD Simulations. *Journal of Geophysical Research (Space Physics)*, *125*(7), e27510. doi: 10.1029/2019JA027510

Genestreti, K. J., Li, X., Liu, Y.-H., Burch, J. L., Torbert, R. B., Fuselier, S. A., ... Strangeway, R. J. (2022, August). On the origin of "patchy" energy conversion in electron diffusion regions. *Physics of Plasmas*, *29*(8), 082107. doi: 10.1063/5.0090275

Glocer, A., Dorelli, J., Toth, G., Komar, C. M., & Cassak, P. A. (2016, January). Separator reconnection at the magnetopause for predominantly northward and southward IMF: Techniques and results. *Journal of Geophysical Research (Space Physics)*, *121*(1), 140-156. doi: 10.1002/2015JA021417

Gonzalez, W. D., & Mozer, F. S. (1974, October). A quantitative model for the potential resulting from reconnection with an arbitrary interplanetary magnetic field. , *79*(28), 4186. doi: 10.1029/JA079i028p04186

Haaland, S., Paschmann, G., Øieroset, M., Phan, T., Hasegawa, H., Fuselier, S. A., ... Burch, J. (2020, March). Characteristics of the Flank Magnetopause: MMS Results. *Journal of Geophysical Research (Space Physics)*, *125*(3), e27623. doi: 10.1029/2019JA027623

Hesse, M., Aunai, N., Zenitani, S., Kuznetsova, M., & Birn, J. (2013, June). Aspects of collisionless magnetic reconnection in asymmetric systems. *Physics of Plasmas*, *20*(6), 061210. doi: 10.1063/1.4811467

Hill, T. W. (1975, December). Magnetic merging in a collisionless plasma. , *80*(34), 4689. doi: 10.1029/JA080i034p04689

Jeandet, A., & Schulz, A. (2023, November). *Speasy [Software].* Retrieved from `https://github.com/SciQLop/speasy` doi: 10.5281/zenodo.7995732

Jelínek, K., Němeček, Z., & Šafránková, J. (2012, May). A new approach to magnetopause and bow shock modeling based on automated region identification. *Journal of Geophysical Research (Space Physics)*, *117*(A5), A05208. doi: 10.1029/2011JA017252

Kaymaz, Z. (1998, April). IMP 8 magnetosheath field comparisons with models. *Annales Geophysicae*, *16*(4), 376-387. doi: 10.1007/s00585-998-0376-3

King, J. H., & Papitashvili, N. E. (2005, February). Solar wind spatial scales in and comparisons of hourly Wind and ACE plasma and magnetic field data. *Jour-*

nal of Geophysical Research (Space Physics), *110*(A2), A02104. doi: 10.1029/2004JA010649

Kobel, E., & Fluckiger, E. O. (1994, December). A model of the steady state magnetic field in the magnetosheath. , *99*(A12), 23617-23622. doi: 10.1029/94JA01778

Komar, C. M., & Cassak, P. A. (2016, June). The local dayside reconnection rate for oblique interplanetary magnetic fields. *Journal of Geophysical Research (Space Physics)*, *121*(6), 5105-5120. doi: 10.1002/2016JA022530

Komar, C. M., Fermo, R. L., & Cassak, P. A. (2015, January). Comparative analysis of dayside magnetic reconnection models in global magnetosphere simulations. *Journal of Geophysical Research (Space Physics)*, *120*(1), 276-294. doi: 10.1002/2014JA020587

Lenouvel, Q., Génot, V., Garnier, P., Toledo-Redondo, S., Lavraud, B., Aunai, N., ... Burch, J. L. (2021, May). Identification of Electron Diffusion Regions with a Machine Learning Approach on MMS Data at the Earth's Magnetopause. *Earth and Space Science*, *8*(5), e01530. doi: 10.1029/2020EA001530

Lin, R. L., Zhang, X. X., Liu, S. Q., Wang, Y. L., & Gong, J. C. (2010, April). A three-dimensional asymmetric magnetopause model. *Journal of Geophysical Research (Space Physics)*, *115*(A4), A04207. doi: 10.1029/2009JA014235

Liu, Y.-H., Hesse, M., Guo, F., Daughton, W., Li, H., Cassak, P. A., & Shay, M. A. (2017, February). Why does Steady-State Magnetic Reconnection have a Maximum Local Rate of Order 0.1? , *118*(8), 085101. doi: 10.1103/PhysRevLett.118.085101

Liu, Y.-H., Hesse, M., & Kuznetsova, M. (2015, September). Orientation of X lines in asymmetric magnetic reconnection—Mass ratio dependency. *Journal of Geophysical Research (Space Physics)*, *120*(9), 7331-7341. doi: 10.1002/2015JA021324

Liu, Y.-H., Hesse, M., Li, T. C., Kuznetsova, M., & Le, A. (2018, June). Orientation and Stability of Asymmetric Magnetic Reconnection X Line. *Journal of Geophysical Research (Space Physics)*, *123*(6), 4908-4920. doi: 10.1029/2018JA025410

Liu, Z. Q., Lu, J. Y., Wang, C., Kabin, K., Zhao, J. S., Wang, M., ... Zhao, M. X. (2015, July). A three-dimensional high Mach number asymmetric magnetopause model from global MHD simulation. *Journal of Geophysical Research (Space Physics)*, *120*(7), 5645-5666. doi: 10.1002/2014JA020961

Luhmann, J. G., Walker, R. J., Russell, C. T., Crooker, N. U., Spreiter, J. R., & Stahara, S. S. (1984, March). Patterns of Potential Magnetic Field Merging Sites on the Dayside Magnetopause. , *89*(A3), 1739-1742. doi: 10.1029/JA089iA03p01739

Lukin, A. S., Panov, E. V., Artemyev, A. V., Petrukovich, A. A., Haaland, S., Nakamura, R., ... Strangeway, R. J. (2020, November). Comparison of the Flank Magnetopause at Near-Earth and Lunar Distances: MMS and ARTEMIS Observations. *Journal of Geophysical Research (Space Physics)*, *125*(11), e28406. doi: 10.1029/2020JA028406

McFadden, J. P., Carlson, C. W., Larson, D., Ludlam, M., Abiad, R., Elliott, B., ... Angelopoulos, V. (2008, Dec). The THEMIS ESA Plasma Instrument and In-flight Calibration. *Scientific Studies of Reading*, *141*(1-4), 277-302. doi: 10.1007/s11214-008-9440-2

Michotte de Welle, B., Aunai, N., Nguyen, G., Lavraud, B., Génot, V., Jeandet, A., & Smets, R. (2022, December). Global Three-Dimensional Draping of Magnetic Field Lines in Earth's Magnetosheath From In-Situ Spacecraft Measurements. *Journal of Geophysical Research (Space Physics)*, *127*(12), e2022JA030996. doi: 10.1029/2022JA030996

Moore, T. E., Fok, M. C., & Chandler, M. O. (2002, October). The dayside reconnection X line. *Journal of Geophysical Research (Space Physics)*, *107*(A10),

1332. doi: 10.1029/2002JA009381

Nguyen, G., Aunai, N., Michotte de Welle, B., Jeandet, A., Lavraud, B., & Fontaine, D. (2022a, January). Massive Multi-Mission Statistical Study and Analytical Modeling of the Earth's Magnetopause: 1. A Gradient Boosting Based Automatic Detection of Near-Earth Regions. *Journal of Geophysical Research (Space Physics)*, *127*(1), e29773. doi: 10.1029/2021JA029773

Nguyen, G., Aunai, N., Michotte de Welle, B., Jeandet, A., Lavraud, B., & Fontaine, D. (2022b, January). Massive Multi-Mission Statistical Study and Analytical Modeling of the Earth's Magnetopause: 4. On the Near-Cusp Magnetopause Indentation. *Journal of Geophysical Research (Space Physics)*, *127*(1), e29776. doi: 10.1029/2021JA029776

Olshevsky, V., Khotyaintsev, Y. V., Lalti, A., Divin, A., Delzanno, G. L., Anderzén, S., ... Markidis, S. (2021, October). Automated Classification of Plasma Regions Using 3D Particle Energy Distributions. *Journal of Geophysical Research (Space Physics)*, *126*(10), e29620. doi: 10.1029/2021JA029620

Onsager, T. G., Thomsen, M. F., Elphic, R. C., & Gosling, J. T. (1991, December). Model of electron and ion distributions in the plasma sheet boundary layer. , *96*(A12), 20999-21011. doi: 10.1029/91JA01983

Pedregosa, F., Varoquaux, G., Gramfort, A., Michel, V., Thirion, B., Grisel, O., ... Duchesnay, E. (2011). Scikit-learn: Machine learning in Python. *Journal of Machine Learning Research*, *12*, 2825–2830.

Petrinec, S. M., Burch, J. L., Fuselier, S. A., Trattner, K. J., Giles, B. L., & Strangeway, R. J. (2022, June). On the Occurrence of Magnetic Reconnection Along the Terrestrial Magnetopause, Using Magnetospheric Multiscale (MMS) Observations in Proximity to the Reconnection Site. *Journal of Geophysical Research (Space Physics)*, *127*(6), e29669. doi: 10.1029/2021JA029669

Phan, T. D., Drake, J. F., Shay, M. A., Gosling, J. T., Paschmann, G., Eastwood, J. P., ... Angelopoulos, V. (2014, October). Ion bulk heating in magnetic reconnection exhausts at Earth's magnetopause: Dependence on the inflow Alfvén speed and magnetic shear angle. , *41*(20), 7002-7010. doi: 10.1002/2014GL061547

Phan, T. D., Freeman, M. P., Kistler, L. M., Klecker, B., Haerendel, G., Paschmann, G., ... Reme, H. (2001, June). Evidence for an extended reconnection line at the dayside magnetopause. *Earth, Planets and Space*, *53*, 619-625. doi: 10.1186/BF03353281

Phan, T. D., Hasegawa, H., Fujimoto, M., Oieroset, M., Mukai, T., Lin, R. P., & Paterson, W. (2006, May). Simultaneous Geotail and Wind observations of reconnection at the subsolar and tail flank magnetopause. , *33*(9), L09104. doi: 10.1029/2006GL025756

Phan, T. D., Kistler, L. M., Klecker, B., Haerendel, G., Paschmann, G., Sonnerup, B. U. Ö., ... Reme, H. (2000, April). Extended magnetic reconnection at the Earth's magnetopause from detection of bi-directional jets. , *404*(6780), 848-850. doi: 10.1038/35009050

Phan, T. D., Paschmann, G., Baumjohann, W., Sckopke, N., & Luehr, H. (1994, January). The magnetosheath region adjacent to the dayside magnetopause: AMPTE/IRM observations. , *99*(A1), 121-142. doi: 10.1029/93JA02444

Phan, T. D., Paschmann, G., Gosling, J. T., Oieroset, M., Fujimoto, M., Drake, J. F., & Angelopoulos, V. (2013, January). The dependence of magnetic reconnection on plasma β and magnetic shear: Evidence from magnetopause observations. , *40*(1), 11-16. doi: 10.1029/2012GL054528

Pollock, C., Moore, T., Jacques, A., Burch, J., Gliese, U., Saito, Y., ... Zeuch, M. (2016, Mar). Fast Plasma Investigation for Magnetospheric Multiscale. *Scientific Studies of Reading*, *199*(1-4), 331-406. doi: 10.1007/s11214-016-0245-4

Pu, Z. Y., Xiao, C. J., Zhang, X. G., Huang, Z. Y., Fu, S. Y., Liu, Z. X., ... Wang, X. G. (2005, November). Double Star TC-1 observations of component

reconnection at the dayside magnetopause: a preliminary study. *Annales Geophysicae*, *23*(8), 2889-2895. doi: 10.5194/angeo-23-2889-2005

Reconnection of magnetic fields: Magnetohydrodynamics and collisionless theory and observations. (2007). Cambridge University Press. doi: 10.1017/CBO9780511536151

Rème, H., Aoustin, C., Bosqued, J. M., Dand ouras, I., Lavraud, B., Sauvaud, J. A., ... Sonnerup, B. (2001, Oct). First multispacecraft ion measurements in and near the Earth's magnetosphere with the identical Cluster ion spectrometry (CIS) experiment. *Annales Geophysicae*, *19*, 1303-1354. doi: 10.5194/angeo-19-1303-2001

Rème, H., Dandouras, I., Aoustin, C., Bosqued, J. M., Sauvaud, J. A., Vallat, C., ... Lundin, R. (2005, November). The HIA instrument on board the Tan Ce 1 Double Star near-equatorial spacecraft and its first results. *Annales Geophysicae*, *23*(8), 2757-2774. Retrieved from `https://hal.archives-ouvertes.fr/hal-00329440`

Romashets, E. P., & Vandas, M. (2019, April). Analytic Modeling of Magnetic Field in the Magnetosheath and Outer Magnetosphere. *Journal of Geophysical Research (Space Physics)*, *124*(4), 2697-2710. doi: 10.1029/2018JA026006

Russell, C. T., Anderson, B. J., Baumjohann, W., Bromund, K. R., Dearborn, D., Fischer, D., ... Richter, I. (2016, Mar). The Magnetospheric Multiscale Magnetometers. *Scientific Studies of Reading*, *199*(1-4), 189-256. doi: 10.1007/s11214-014-0057-3

Safránková, J., Nemecek, Z., Dusík, S., Prech, L., Sibeck, D. G., & Borodkova, N. N. (2002, March). The magnetopause shape and location: a comparison of the Interball and Geotail observations with models. *Annales Geophysicae*, *20*(3), 301-309. doi: 10.5194/angeo-20-301-2002

Schreier, R., Swisdak, M., Drake, J. F., & Cassak, P. A. (2010, November). Three-dimensional simulations of the orientation and structure of reconnection X-lines. *Physics of Plasmas*, *17*(11), 110704-110704. doi: 10.1063/1.3494218

Scurry, L., Russell, C. T., & Gosling, J. T. (1994, August). A statistical study of accelerated flow events at the dayside magnetopause. , *99*(A8), 14,815-14,829. doi: 10.1029/94JA00793

Shue, J. H., Song, P., Russell, C. T., Steinberg, J. T., Chao, J. K., Zastenker, G., ... Kawano, H. (1998, August). Magnetopause location under extreme solar wind conditions. , *103*(A8), 17691-17700. doi: 10.1029/98JA01103

Sibeck, D. G., Lopez, R. E., & Roelof, E. C. (1991, April). Solar wind control of the magnetopause shape, location, and motion. , *96*(A4), 5489-5495. doi: 10.1029/90JA02464

Sonnerup, B. U. Ö. (1974, April). Magnetopause reconnection rate. , *79*(10), 1546-1549. doi: 10.1029/JA079i010p01546

Souza, V. M., Gonzalez, W. D., Sibeck, D. G., Koga, D., Walsh, B. M., & Mendes, O. (2017, April). Comparative study of three reconnection X line models at the Earth's dayside magnetopause using in situ observations. *Journal of Geophysical Research (Space Physics)*, *122*(4), 4228-4250. doi: 10.1002/2016JA023790

Sun, W., Slavin, J. A., Nakamura, R., Heyner, D., Trattner, K. J., Mieth, J. Z. D., ... Saito, Y. (2022, April). Dayside magnetopause reconnection and flux transfer events under radial interplanetary magnetic field (IMF): Bepi-Colombo Earth-flyby observations. *Annales Geophysicae*, *40*(2), 217-229. doi: 10.5194/angeo-40-217-2022

Swisdak, M., & Drake, J. F. (2007, June). Orientation of the reconnection X-line. , *34*(11), L11106. doi: 10.1029/2007GL029815

Swisdak, M., Rogers, B. N., Drake, J. F., & Shay, M. A. (2003, May). Diamagnetic suppression of component magnetic reconnection at the magnetopause. *Journal of Geophysical Research (Space Physics)*, *108*(A5), 1218. doi:

10.1029/2002JA009726

Toledo-Redondo, S., André, M., Aunai, N., Chappell, C. R., Dargent, J., Fuselier, S. A., ... Vines, S. K. (2021, September). Impacts of Ionospheric Ions on Magnetic Reconnection and Earth's Magnetosphere Dynamics. *Reviews of Geophysics*, *59*(3), e00707. doi: 10.1029/2020RG000707

Trattner, K. J., Burch, J. L., Ergun, R., Eriksson, S., Fuselier, S. A., Giles, B. L., ... Wilder, F. D. (2017, December). The MMS Dayside Magnetic Reconnection Locations During Phase 1 and Their Relation to the Predictions of the Maximum Magnetic Shear Model. *Journal of Geophysical Research (Space Physics)*, *122*(12), 11,991-12,005. doi: 10.1002/2017JA024488

Trattner, K. J., Burch, J. L., Ergun, R., Fuselier, S. A., Gomez, R. G., Grimes, E. W., ... Young, D. T. (2016, May). The response time of the magnetopause reconnection location to changes in the solar wind: MMS case study. , *43*(10), 4673-4682. doi: 10.1002/2016GL068554

Trattner, K. J., Mulcock, J. S., Petrinec, S. M., & Fuselier, S. A. (2007, February). Location of the reconnection line at the magnetopause during southward IMF conditions. , *34*(3), L03108. doi: 10.1029/2006GL028397

Trattner, K. J., Petrinec, S. M., & Fuselier, S. A. (2021, April). The Location of Magnetic Reconnection at Earth's Magnetopause. , *217*(3), 41. doi: 10.1007/s11214-021-00817-8

Trattner, K. J., Petrinec, S. M., Fuselier, S. A., Omidi, N., & Sibeck, D. G. (2012a, January). Evidence of multiple reconnection lines at the magnetopause from cusp observations. *Journal of Geophysical Research (Space Physics)*, *117*(A1), A01213. doi: 10.1029/2011JA017080

Trattner, K. J., Petrinec, S. M., Fuselier, S. A., Omidi, N., & Sibeck, D. G. (2012b, January). Evidence of multiple reconnection lines at the magnetopause from cusp observations. *Journal of Geophysical Research (Space Physics)*, *117*(A1), A01213. doi: 10.1029/2011JA017080

Tsyganenko, N. A., & Stern, D. P. (1996, December). Modeling the global magnetic field of the large-scale Birkeland current systems. , *101*(A12), 27187-27198. doi: 10.1029/96JA02735

van der Walt, S., Schönberger, J. L., Nunez-Iglesias, J., Boulogne, F., Warner, J. D., Yager, N., ... the scikit-image contributors (2014, 6). scikit-image: image processing in Python. *PeerJ*, *2*, e453. Retrieved from `https://doi.org/10.7717/peerj.453` doi: 10.7717/peerj.453

Vasyliunas, V. M. (1975, February). Theoretical models of magnetic field line merging, 1. *Reviews of Geophysics and Space Physics*, *13*, 303-336. doi: 10.1029/RG013i001p00303

Walsh, B. M., Komar, C. M., & Pfau-Kempf, Y. (2017, April). Spacecraft measurements constraining the spatial extent of a magnetopause reconnection X line. , *44*(7), 3038-3046. doi: 10.1002/2017GL073379

Zhang, H., Fu, S., Pu, Z., Lu, J., Zhong, J., Zhu, C., ... Liu, L. (2019, August). Statistics on the Magnetosheath Properties Related to Magnetopause Magnetic Reconnection. , *880*(2), 122. doi: 10.3847/1538-4357/ab290e

Zhou, M., Ashour-Abdalla, M., Deng, X., Pang, Y., Fu, H., Walker, R., ... Tang, R. (2017, September). Observation of Three-Dimensional Magnetic Reconnection in the Terrestrial Magnetotail. *Journal of Geophysical Research (Space Physics)*, *122*(9), 9513-9520. doi: 10.1002/2017JA024597